

1 **The emergent Yo-yo movement of nuclei driven by collective**
2 **cytoskeletal remodeling in pseudo-synchronous mitotic cycles**

3

4 Zhiyi Lv^{1, 7, 8, 9}, Jan Rosenbaum², Stephan Mohr³, Xiaozhu Zhang⁴, Deqing
5 Kong^{1, 6}, Helen Preiß⁵, Sebastian Kruss⁵, Karen Alim³, Timo Aspelmeier²,
6 Jörg Großhans^{1, 6}

7

8 1. Institut für Entwicklungsbiochemie, Universitätsmedizin, Georg-August-
9 Universität Göttingen, Germany.

10 2. Institut für Mathematische Stochastik, Georg-August-Universität Göttingen,
11 Germany.

12 3. Germany Max Planck Institute for Dynamics and Self-Organization,
13 Göttingen, Germany,

14 4. Chair for Network Dynamics, Institute for Theoretical Physics and Center
15 for Advancing Electronics Dresden (cfaed), Cluster of Excellence Physics of
16 Life, TU Dresden, 01062 Dresden,

17 5. Institut für Physikalische Chemie, Georg-August-Universität Göttingen,
18 Germany

19 6. Fachbereich Biologie, Philipps-Universität Marburg, Germany

20 7. Institute of Evolution and Marine Biodiversity, Ocean University of China,
21 Qingdao, 266003, China.

22 8. Ministry of Education Key Laboratory of Marine Genetics and Breeding,
23 College of Marine Life Sciences, Ocean University of China, Qingdao,
24 266003, China

25 9. Laboratory for Marine Biology and Biotechnology, Qingdao National
26 Laboratory for Marine Science and Technology, Qingdao, 266237, China.

27

28

29 corresponding author:

30 Zhiyi Lv

31 lv.zhiyi@med.uni-goettingen.de

32 Jörg Großhans

33 jgrossh@gwdg.de

34

35 **Abstract:**

36 Many aspects in tissue morphogenesis are attributed to the collective
37 behavior of the participating cells. Yet, the mechanism for emergence of
38 dynamic tissue behavior is not understood completely. Here we report the “yo-
39 yo”-like nuclear drift movement in *Drosophila* syncytial embryo displays typical
40 emergent feature of collective behavior, which is associated with pseudo-
41 synchronous nuclear division cycle. We uncover the direct correlation
42 between the degree of asynchrony of mitosis and the nuclear collective
43 movement. Based on experimental manipulations and numerical simulations,
44 we find the ensemble of spindle elongation, rather than a nucleus’ own
45 spindle, is the main driving force for its drift movement. The cortical F-actin
46 acts as viscoelastic medium to dampen the movements and plays a critical
47 role in restoring the nuclear positions after a mitosis cycle. Our study provides
48 insights into how the interactions between cytoskeleton as individual elements
49 leads to collective movement of the nuclear array on a macroscopic scale.

50

51 **Keywords:** syncytium, nuclear array, cortex, microtubule, F-actin, formin, Dia,
52 network, emergent behavior, ELMO, flow, biomechanics

53

54 Introduction

55

56 Collective behaviors emerge from many interacting individuals in the absence
57 of central coordination and supervision. Birds flocks, fish schools, as well as
58 bacterial colonies exhibit spontaneous synchronization and many other
59 complex dynamic functional patterns originating from simple local interaction
60 rules [1-3]. Within a single organism, self-organized collective behaviors are
61 an inseparable part in maintaining its basic biological functions by efficiently
62 driving numerous complex biological processes without external regulations
63 such as neural activation in brain [4-6] and morphogenesis during embryonic
64 development [7,8]. On subcellular scale, actin and microtubules form
65 collective motion in the presence of motor proteins and ATP [9-11]. Yet,
66 despite the ubiquitousness and the significance of emergent collective
67 behavior in biology, our knowledge of the fundamental mechanism of
68 functional collective behaviors are very limited. The major obstacle lies in the
69 typically extremely complex interactions between the individuals in most
70 biological collective behaviors. However, in syncytial insect embryo only direct
71 cytoskeletal interactions exist, owing to the lack of membranes separating the
72 nuclei, which enables dissecting and understanding how the interactions of
73 individuals drive the formation of emergent features at tissue level.

74

75 To obtain insights into the molecular mechanism leading to the emergence of
76 a collective flow movement, we study the dynamics of nuclear array in
77 *Drosophila* syncytial blastoderm, where the direct interactions between
78 individuals lead to at least three features of emergent collective behavior
79 observed at tissue level. Firstly, the nuclei divide synchronously to their
80 immediate neighbors but asynchronously to more distant nuclei. This leads to
81 a wave front of mitosis sweeping over the embryo [12,13]. Secondly, the
82 nuclei arrange in an ordered array in interphase following disturbance during
83 nuclear division. Ordering involves interactions by the microtubule asters but
84 also with F-actin at the cortex [14,15]. Thirdly, the nuclei and the cytoplasm
85 undergo stereotypic flow movements following the mitotic wave, which is
86 reminiscent of the toy “yo-yo”. This arises the questions: how does the flow
87 emerge and what are the underlying driving forces? Is there any physiological
88 function of this flow?

89

90 The large-scale collective movements are driven by active elements of the
91 cytoskeleton. For example, kinesin-1 and microtubules drive the cytoplasmic
92 streaming during *Drosophila* oogenesis [16]. The cytoplasmic streaming in
93 plant and algae is driven by myosins moving on F-actin [17,18]. Apical
94 constriction mediated by actomyosin can generate the cytoplasmic flow, which

95 compels nuclear spreading in *Drosophila* pre-blastoderm [19] and cell
96 elongation in gastrulation [20].

97

98 In *Drosophila* syncytial blastoderm, the nuclei and their associated
99 centrosomes and microtubule asters form an extended two-dimensional array
100 [14]. The dynamics of this array is dominated by two different interactions [21].
101 Lateral interactions between the neighbor nuclei and centrosomes are
102 mediated by microtubules and the associated motor proteins. The interactions
103 between centrosomes and actin cortex constitute the cortical interactions.
104 How these interactions lead to the stereotypic nuclear movement is unknown.

105

106 Beside the force generating mechanism, the material properties of the
107 embryos [22-24] may influence the movement of the nuclei. The actin
108 cytoskeleton inhibits short time-scale movements [21] and promotes ordering
109 of the nuclear array [14]. The actin cortex may act as a viscoelastic medium,
110 to which the centrosomes and their associated nuclei are connected.

111

112 Here we found that the nuclear movement was isotropic for individual spindles
113 but anisotropic for the collective flow over several nuclear diameters away
114 from the mitotic wave front and back to the original position slightly later. We
115 comprehensively quantified nuclear trajectories in wild type and mutant
116 embryos and modelled the process by computational simulation. In this way,
117 we uncovered that the ensemble of spindle elongation, rather than a nucleus'
118 own spindle, is the main driving force for its drift movement. In addition, we
119 defined a function of cortical F-actin for the apparent viscoelastic material
120 properties to restore the nuclear position. Lastly, based on a simulation, we
121 proposed that such nuclear movement is prerequisite for nuclear division in
122 high density in *Drosophila* syncytial blastoderm.

123

124 **Results**

125

126 **Collective flow and density changes follow the mitotic wave front of 127 pseudo-synchronous nuclear cycles**

128 To elucidate the mechanisms that arise the emergent features of nuclear
129 array dynamics in *Drosophila* syncytial cleavage cycle, we first documented
130 nuclear division cycles using time-lapse microscopy. The nuclei divide slightly
131 asynchronous especially during the last syncytial division in NC13 with a time
132 lag of up to minutes, which is easily visible as a mitotic wave front sweeping
133 over the embryo (Fig. 1A, Supp. Data Fig. S1A, Movie 1). The mitotic wave is
134 driven by Cdk1 activity wave and the molecular processes of the how the
135 chemical wave propagates were dissected [12,25].

136 The mitotic pseudo-synchrony and its corresponding wave front are
137 associated with a stereotypic nuclear movement, which can be readily
138 observed in time lapse movies (Fig. 1B, C, Supp. Data Movie 2). To obtain a
139 precise description of the nuclear movements, we determined the trajectories
140 of all nuclei within the field of view from time lapse recordings of fluorescently
141 labeled nuclei. From the trajectories, we extracted time courses for
142 displacements, velocities, and nuclear density (Fig. 1D, E, Supp. Data Fig.
143 S1B, C). Every nucleus is assigned an individual time axis with the splitting of
144 daughter chromosomes (metaphase-anaphase transition) as reference time
145 $t=0$.

146
147 Concerning displacement (Fig. 1D), the nuclei moved in average about 20 μm
148 which corresponds to about 4–5 nuclear diameters away from the position of
149 their mother nucleus at $t=0$. The maximal displacement was reached after
150 about 2 min (Fig. 1D). Following maximal displacement, the nuclei then
151 returned to almost their initial position. This movement resembles yo-yo ball,
152 and hereafter we refer it as yo-yo movement. We calculated the speed of
153 nuclear movement from the individual trajectories as the derivative of the
154 trajectories. The averaged flow speed revealed three peaks (Fig. 1E). The first
155 peak corresponds to the chromosome segregation in anaphase with about 0.4
156 $\mu\text{m/s}$. The second peak after about 1 to 2 min corresponds to the flow away
157 from the mitotic wave front. The least pronounced, third peak corresponds to
158 the return movement after about 4 min.

159
160 Asynchronicity of mitosis might be prerequisite for yo-yo flow. To test whether
161 there is a correlation, we collected data from 50 embryos (Fig. S1A) for
162 quantification of the speed of wave front and maximal displacement. Plotting
163 corresponding parameter sets revealed a negative correlation ($R^2=45\%$, Fig.
164 1F), which suggests a slow wave is associated with a large displacement.

165
166 As flow is linked to density changes, we next established spatial and temporal
167 maps of nuclear density. Each nucleus was assigned an area and
168 corresponding density according to Voronoi segmentation (Supp. Data Fig.
169 S1B, Movie 3). In the case of synchronous divisions, the density would be
170 expected to double at $t=0$ (metaphase anaphase transition) and remain
171 constant throughout interphase. In contrast, but consistent with the observed
172 nuclear flow, our measurements revealed a peculiar time of the density.
173 Although initially doubling, the density dropped in telophase before finally
174 reaching the doubled density again a few minutes later (Supp. Data Fig. S1B,
175 C). Corresponding profiles for displacement and flows were detected in
176 preceding nuclear cycles 11 and 12, although in a less pronounced manner
177 (Supp. Data Fig. S2).

178

179 The forth and back movement of the nuclei is reminiscent of a spring (Supp.
180 Data Fig. S1D). To obtain a phenomenological description of this behavior, we
181 applied a simple mechanical model to the nuclear trajectories during the
182 period of maximal displacement. By fitting a square function to the
183 displacement curve, we obtained an apparent spring constant for each
184 nucleus (Supp. Data Fig. S1E). The actual value of the apparent spring
185 constant is not informative, since our model and assumptions are too simple.
186 Friction is not included, for example. Yet, the apparent constant helps to
187 compare experimental conditions and mutant phenotypes.

188

189 **Isotropic individual behavior is associated with an anisotropic collective** 190 **flow**

191 Our analysis revealed a collective directional flow of the nuclear array. Yet the
192 individual spindles are isotropically oriented. The axes between daughter
193 nuclei are uniformly distributed over the angles against the anterior-posterior
194 axis of the embryo (Fig. 2A–C). In contrast, the same nuclei almost
195 unidirectionally moved along the embryonic axis a minute later, indicating an
196 anisotropic behavior (Fig. 2A–C). The transition of isotropic individual to
197 anisotropic collective behavior is strikingly obvious in the extreme cases of
198 spindle orientation. In the case of a spindle oriented in parallel to the
199 embryonic axis, one set of chromosomes segregated towards, whereas the
200 daughter chromosomes moved away the wave front during anaphase. One
201 minute later both nuclei moved away from the wave front (Fig. 2D). Similarly,
202 in case of a perpendicular orientation of chromosome segregation, the
203 movement during anaphase was perpendicular to the embryonic axis but
204 along the axis a minute later during collective flow. (Fig. 2D).

205

206 The uncoupling of spindle behavior and nuclear behavior was seen not only in
207 the orientation of the movements, but also in the time course of the two
208 behaviors. The maximal displacement was reached only about 1.5 min after
209 the maximal distance between daughter nuclei (maximal spindle length) was
210 reached (Fig. 2E, F), suggesting the maximal displacement was achieved
211 when the nuclei are in telophase. These findings demonstrated that these two
212 processes were mechanistically not directly linked at the individual level, since
213 spindles were isotropically oriented and preceded the flow behavior (Fig. 2G).

214

215 During collective flow the nuclei may move as individuals characterized by
216 neighbor exchanges. Alternatively, nuclei may behave as an array, which
217 would be indicated by fixed neighbor relationships. To distinguish these
218 options, we labeled groups of cells before mitosis and followed them during
219 the course of chromosome segregation and collective flow. We found that the

220 nuclei moved as an array. The groups of nuclei did neither intersperse with
221 unlabeled nuclei nor nuclei of the other groups indicating that neighbor
222 relationships were maintained during mitosis and collective flow despite the
223 movement over several nuclear diameters (Supp. Data Fig. S3A). In addition,
224 we measured the displacement fields of nuclei using a particle image velocity
225 algorithm. We found that the nuclei motion is similar to a laminar flow (Supp.
226 Data Fig. S3B, Movie 4). In summary, our observations indicate that the
227 nuclear layer phenomenologically behaves like an elastic sheet with fixed
228 neighbor relationships.

229

230 **Computational modeling of nuclear movement**

231 To gain a better understanding for how the isotropic spindles gives rise to an
232 anisotropic collective flow, we conducted computational simulations. Starting
233 from a computer model for static nuclear interactions in interphase [15], we
234 added a time axis for the interactions. The model is based on active and
235 passive forces (Fig. 3A). Stochastic active forces repulse adjacent nuclei, thus
236 resembling the sliding activity of motor proteins, e. g. Kinesin-5, on antiparallel
237 aligned microtubules. In addition, a passive elastic force leads to repulsion
238 accounting for the embedding of the nuclei into the cytoplasm and
239 cytoskeleton. This may include the link of the nuclei to the cortex.

240 Chromosome segregation is triggered at $t=0$ by a separation force acting
241 between the daughter nuclei. The interaction forces are dynamic according to
242 the mitotic stage and interphase (Supp. Data Fig. S4). For example, the active
243 force is low in anaphase, since astral microtubules prominently appear only in
244 telo- and interphase. Similarly, the passive force increases in telo- and
245 interphase as cortical actin increases during these stages. The segregation
246 force decays in telo and interphase. Balancing the magnitude of passive and
247 active forces over time, model simulation reproduced the experimentally
248 observed stereotypic flow behavior (Fig. 3B, C, Supp. Data Movie 5).

249

250 Strikingly, the simulations reproduce other features of nuclear yo-yo
251 movement. Firstly, maximal spindle length precedes maximal displacement
252 with a time lag of 1.5 min (Fig. 3D, E vs Fig. 2E, F). Secondly, the speed of
253 the mitotic wave front is negatively correlated with the nuclear maximal
254 displacement (Fig. 3F vs Fig. 1F). In addition, the simulations predict no
255 collective movement of nuclei with asynchronous nuclear divisions in a “salt-
256 and-pepper” pattern (Fig. 3G). Importantly, the simulations predict that the
257 force for separation of the daughter nuclei positively correlates with maximal
258 distance between daughter nuclei and importantly with maximal displacement
259 (Fig. 3H). Thus, our simulations predict that spindle elongation is a major
260 driving force for nuclear movement. Mechanistically, this is not a simple

261 relationship because spindles are isotropically oriented, whereas the direction
262 of displacement is anisotropic.

263

264 **Ensemble spindle elongation is the driving force for nuclear** 265 **displacement**

266 To test the prediction that spindle elongation drives the yo-yo movement, we
267 performed the laser cutting on single spindle. However, the spindle recovered
268 in second-scale and no effects on nuclear motion (Supp. Data Fig. S5). To
269 circumvent this problem, we developed a method to reduce the spindle length
270 globally, without hampering the nuclear separation. Spindle elongation in
271 anaphase B requires the four-headed microtubule motor Kinesin 5, which can
272 slide microtubules against each other [26]. We employed embryos, in which
273 endogenous Kinesin 5 was substituted by a version susceptible to TEV
274 protease [27]. We titrated the amount of TEV protease to achieve a partial
275 depletion which still allowed completion of mitosis. Spindles in these embryos
276 were short (Fig. 4A). The average maximal spindle length was 8 μm instead
277 of 10 μm in wild type embryos. Complementary, we employed embryos from
278 females homozygous for *Map60*, which also displayed short spindles [14] with
279 an average length of 9 μm (Fig. 4A). Quantification of nuclear movement
280 revealed a strongly reduced maximal displacement in both experimental
281 conditions and thus a positive correlation of spindle length and maximal
282 displacement (Fig. 4B, C, D). In summary, analysis of mutant embryos with
283 shorter division distance support an ensemble spindle elongation constitutes a
284 major driving force for the nuclear movement thereafter.

285

286 **F-actin cortex is required for the return movement.**

287 The simulation predicts a function of passive force in yo-yo movement.
288 Cortical F-actin is a promising candidate. It has been previously reported that
289 the nuclei are strongly attached to F-actin cortex [28]. The actin cortex
290 suppresses the fluctuation movements of centrosomes [21] and contributes to
291 an ordered nuclear array in interphase [14]. Cortical F-actin undergoes
292 stereotypic remodeling during the course of nuclear cycles [29] (Fig. 4E,
293 Supp. Data Fig. S6A). We quantified total F-actin with a Utrophin-GFP as a
294 marker [30]. We found that the signal dropped in mitosis, with lowest level
295 during anaphase and steadily increased afterwards (Supp. Data Fig. S6A, B).
296 Given the timing of this dynamics, it is conceivable that cortical actin plays an
297 important part in controlling nuclear movement.

298

299 To test this conceivable function of the cortical F-actin, we employed two
300 mutants to genetically interfere with the organization of the actin cortex (Fig4.
301 F, Supp. Data Fig. S6G). Firstly, we prevented the formation of actin caps with
302 the mutant *ELMO* [21,31]. *ELMO* forms part of an unconventional guanylyl

303 nucleotide exchange factor, which activates Rac signaling in a complex with
304 Sponge/DOCK [32]. *ELMO* mutants lack any actin caps and are characterized
305 by a uniformly structured cortical F-actin [21] (Supp. Data Fig. S6G).
306 Secondly, we employed *dia* mutants [33-35]. Dia is a founding member of the
307 formin family, which nucleate and polymerize linear actin filaments. *dia*
308 mutants lack metaphase furrows but contain actin caps [33] (Supp. Data Fig.
309 S6G).

310
311 We applied our quantitative assay to *ELMO* embryos. A strongly increased
312 nuclear mobility was obvious in time lapse movies (Fig. 4G). Quantification of
313 nuclear trajectories revealed a maximal nuclear displacement of 60 μm as
314 compared to 20 μm in wild type embryos (Fig. 4H, Supp. Data Fig. S6H). In
315 addition to the threefold increased displacement, we observed as a second
316 phenotype that the nuclei did not return to their initial position in *ELMO*
317 mutants (Fig. 4G, H). The impaired back movement indicates a loss of the
318 spring-like behavior. Consistently, we calculated an almost 10-fold reduced
319 spring constant at the turning point of the nuclear trajectories (Supp. Data Fig.
320 S6I). A similar behavior and profiles were detected in NC12 of *ELMO* embryos
321 (Supp. Data Fig. S6J, K).

322
323 We also detected changes in nuclear movement in *dia* mutants. Similar to
324 *ELMO* mutants, we observed a loss of the spring-like back movement. The
325 nuclei did not return to their initial position and the spring constant was almost
326 10-fold reduced (Fig. 4I, J, Supp. Data Fig. S6H, I). In contrast to *ELMO*, the
327 maximal displacement was similar to wild type indicating that the
328 stabilizing/viscos function of the cortex does not depend on *dia*. The
329 neighborhood relationships were largely maintained in *dia* and *ELMO*
330 embryos (Supp. Data Fig. S7). In summary, by employing two mutants
331 affecting F-actin organization, we identified distinct functions of the actin
332 cortex. F-actin is required for the back movement as revealed by the reduced
333 apparent spring constant and the permanent displacement. The *ELMO*-
334 dependent organization into caps appears to be important for limiting nuclear
335 movement.

336

337 **Long mitotic spindles and distance between daughter nuclei require** 338 **pseudo-synchronous nuclear cycles**

339

340 To obtain the further insight into the mitotic wave and consequent yo-yo
341 movement in syncytial embryo, we documented the nuclear separation profile.
342 We found that in mitosis the daughter nuclei are separated by an
343 overshooting spindle, which pushes apart the daughter nuclei more than the
344 average inter-nuclear distance (Fig. 5A, B). With every division during the

345 syncytial blastoderm (nuclear cycles NC 10–13), the nuclear density at the
346 cortex doubles (Supp. Data Fig. S8). The nuclei divide in a wave manner
347 especially during the last syncytial division. The mitotic wave is driven by
348 Cdk1 activity wave, and the activity of DNA replication checkpoint is important
349 in the slowdown of the wave, which occurs in later cycles [12,25]. However,
350 the function of this pseudo-synchrony and the consequent yo-yo movement is
351 unknown. Given the increase of asynchrony with nuclear density, we
352 speculated that spindle overshooting with nuclear crowding may pose a
353 problem for synchronous divisions.

354

355 To test this hypothesis, we employed the *mei41 zld* double mutant embryos
356 [36], as well as the *grp nmk* double mutant embryos [12], to experimentally
357 reduce the nuclear division time in cycle 13. We planned to check how much
358 the spindles were able to elongate in a similar level of nuclear crowding as in
359 wild type embryo, but with a more synchronous division manner.
360 Unfortunately, the chromosomes were not separated at cycle 13 in these
361 mutant embryos (Supp. Data Fig. S9). To circumvent this problem, we
362 simulated nuclear divisions within a limited area. We assigned each nucleus
363 and mitotic spindles a protected area representing the entity in real embryos
364 (Fig. 5C). After chromosome division, the daughter nuclei were pushed apart
365 until reaching the protected area of a neighboring spindles/pair of daughter
366 nuclei, thus assessing the maximal possible distance between daughter nuclei
367 (maximal spindle length). We assumed synchronous divisions and symmetric
368 spindles with isotropic orientations (Fig. 5D). Our simulations showed that the
369 maximal spindle length decreased with an increase in nuclear number and
370 thus marked the transition line between structurally allowed and forbidden
371 regime of combinations of nuclear density and spindle length (Fig. 5E). Next,
372 we measured the maximal distance between daughter nuclei and their
373 corresponding nuclear densities in wild type embryos. We also included data
374 from haploid embryos, which undergo an extra nuclear division. Only the
375 parameters of NC11 fell into the allowed area, whereas the parameters of
376 NC12, NC13, and NC14 in haploids fell into the forbidden regime. This
377 analysis indicated that a synchronous division with the observed spindle
378 lengths was possible only in the early cycles but impossible in later cycles.
379 Thus, pseudo-synchrony allows for the observed spindle length in NC12,
380 NC13 and NC14 in haploid embryos.

381

382 **Discussion**

383 The direct interactions between the nuclei and their associated cytoskeleton
384 are a special feature of syncytial embryos. Due to the lack of separating cell
385 membranes, microtubule asters originating from the centrosomes associated
386 with each nucleus form an extended network of hundreds to thousands of

387 elements. Emergent features arise in this network by summing up the
388 behavior of individual elements, such as fluctuations or duplication, and their
389 interactions, such as repulsion. The analysis of the mechanism underlying the
390 emergent features is essential for understanding how the individual cells
391 function collectively to form a tissue.

392

393 We identified an anisotropic flow of the nuclear array as an emergent feature.
394 Based on a morphodynamical analysis of the nuclear array in wild type and
395 mutant embryos together with computational simulations, we analyzed the
396 mechanism of the flow behavior. In this way we identified spindle elongation
397 drives nuclei moving away whereas cortical F-actin restores the nuclear
398 positions, which is necessary for the following development. The emergent
399 nature of the nuclear flow becomes obvious, since individual behavior is
400 strikingly different than the collective behavior of the nuclear array. Nuclei
401 divide with an isotropic orientation, whereas the flow direction is anisotropic.
402 Furthermore, the maximal division distance is about 10 μm , whereas the
403 maximal displacement is about 20 μm .

404

405 In addition to the driving force of the nuclear yo-yo movement, our “limited
406 area” simulation (Fig. 5C, D, E) demonstrates the necessity of such
407 movement. To complete the nuclear division in a limited space with high
408 nuclear density, two strategies could be utilized. The first strategy is to reduce
409 the spindle length, as what happens in *Map60* mutant and Kinesin-5 partially
410 depleted embryos. This might raise the risk that the genetic materials cannot
411 separate completely. The second strategy is that nuclei divide in an
412 asynchronous manner. Besides *Drosophila*, the nuclear division asynchrony
413 was observed in beetle *Tribolium castaneum* [37], implying this might be a
414 conserved mechanism in insect syncytial embryos. The nuclear directional
415 movement is the consequence of the asynchronous divisions. With strongly
416 synchronous divisions, the pushing forces of mitotic spindles would generate
417 a spatially isotropic force distribution. Consequently, the nuclei would not
418 move due to a balance in forces. However, in the case of pseudo-
419 synchronous divisions, the force balance is broken leading to an imbalance
420 and thus a flow away from the wave front. The repulsive force between
421 daughter nuclei increases in anaphase pushing the daughter nuclei apart,
422 followed by a drop in telophase due to spindle disassembly (Supp. Data Fig.
423 S11A). The summing up of all nuclei in an embryo at a given mitotic time
424 results in an asymmetric force field, which likely determines the directionality
425 of the nuclear flow in telophase (Supp. Data Fig. S11B).

426

427 Upon the nuclei reach the maximal displacements, they return to the starting
428 positions. Consistency of nuclear position among different cleavage cycles is

429 important for maintaining the positioning information provided by morphogens.
430 We identified a contribution of the actin cortex to the viscoelastic feature of the
431 nuclear movement, i.e. that nuclei return to their starting position. This is
432 consistent with previous findings that the elasticity of *Drosophila* embryonic
433 cortex in cellularization stage depends on the actin cytoskeleton [23,24]. In
434 addition, the structure of actin cortex is undergoing remodeling, which may
435 contribute to the returning movements by actively changing the cortical
436 material properties in time and space.

437 Collective behaviors driven by the integration of forces originated from
438 cytoskeletal networks are indispensable in biological systems. Some basic
439 ingredients of the system — the mechanical properties of the cytoskeleton
440 and the function of motor proteins have been well studied *in vitro*. The
441 morphology of early *Drosophila* embryos has also been extensively imaged.
442 However, the assembly of the puzzle to achieve a quantitative understanding
443 of the molecular mechanics behind the dynamical self-organization of the
444 rapidly developing embryo, has only begun to be explored. Our study of the
445 dynamical properties of the syncytial embryo is a first step towards our long-
446 term goal to understand how cells mechanically interact with each other and
447 collectively function as active matter forming a tissue.

448 **Methods and Materials**

449 ***Drosophila* Genetics**

450 Fly stocks were obtained from the Bloomington *Drosophila* Stock Center
451 [38,39], unless otherwise noted. Fly strains used in this study are the
452 followings: *w*; Histone2Av-GFP. *w*; mCherry-Tubulin, Histone2Av-GFP. *w*;
453 *sqh-Utr-GFP/CyO*; *ubi-His2Av-RFP*[30]. *Map60^{KG00506}*. *w*; *ubi-GFP-D-Cad dia⁵*
454 *Frt^{2L} ubi-His2Av-RFP/CyO* [33]. *w*; *ELMO³⁶⁷ Frt^{2L}/CyO* [21]. *w Hira^{ssm}/FM7c*,
455 *w^a B* [40]. *His2Av-RFP*; *Kinesin5-[TEV]-GFP* [27]. *mei41 zld/FM7* [36]. *grp*
456 *nmk*. *Sqh-GFP*, *Histone2Av-GFP*. Fly stocks were kept at 25°C on a standard
457 cornmeal food. Germline clones of *dia* and *ELMO* were induced by crossing
458 with corresponding *Frt* chromosomes and the following heat shock at 37°C for
459 one hour on two consecutive days after hatching.

460

461 **Phalloidin staining and imaging**

462 Wild type embryos and embryos from *dia* and *ELMO* germline clones were
463 fixed with 8% formaldehyde according to standard procedures. The vitelline
464 membrane was manually removed. Fixed embryos were incubated with
465 phalloidin-Alexa 488 (1:500, Thermo Fisher) for 1.5 h. After rinsing three times
466 and washing three times for 15 min each with PBT (PBS(Phosphate-Buffered
467 Saline) with 0.1% Tween 20), embryos were stained with DAPI (4',6-
468 Diamidine-2'-phenylindole dihydrochloride) (0.2 µg/ml) for 10 min, rinsed three
469 times in PBT, washed in PBT for 10 min and mounted in Aqua-Poly/Mount

470 (Polysciences). The images of fixed embryos were acquired using a Zeiss
471 LSM780 confocal microscope.

472

473 **Microinjection**

474 1–2 h old embryos were collected, dechorionated with 50% bleach solution for
475 90 s, rinsed thoroughly with deionized water. After aligning on a coverslip, the
476 embryos were desiccated for 10 min, and covered with halocarbon oil
477 (Voltalet 10S, Lehmann & Voss). TEV protease (a gift from Dirk Görlich) and
478 Histone1-Alexa-488 protein (2 mg/ml, Thermo Fisher) were injected to the
479 desired embryos using Microinjector FemtoJet® (Eppendorf) on an inverted
480 microscope. Short spindle was induced by TEV injection in to the embryos
481 expressing Histone2Av-RFP and Kinesin5-[TEV]-GFP. To get the right
482 concentration of TEV protease for injection, we injected TEV with a serial
483 dilution that covers a range of concentration from 10 μM to 0.1 μM . We found
484 1 μM was robust to achieve a partial depletion allowing mitosis but with shorter
485 spindles during the cleavage cycle.

486

487 **Live imaging for nuclear dynamics**

488 Nuclear dynamics was recorded by movies of embryos with the fluorescently
489 labeled nuclei, by expression of Histone2Av-GFP or injection of Histone1-
490 Alexa-488 protein. Embryos were attached on a coverslip coated with embryo
491 glue and covered with halocarbon oil. Time-lapse images were recorded on a
492 spinning disc microscope (Zeiss, 25x/NA0.7 multi immersion) with an emCCD
493 camera (Photometrics, Evolve 512). To ensure reliable tracking of the nuclei,
494 the frame rate was 0.5–0.2 Hz with 4 axial sections, covering 8 μm . Images
495 were merged maximal intensity projections (Fiji/ImageJ[41]).

496

497 **Images process and quantification**

498 Imaging segmentation and analysis were performed with custom-written
499 Python algorithms. The software code is available on request. Briefly, the
500 nuclear positions were detected as blob-like features of size σ_i at position
501 (x_i, y_i) by finding the maxima (x_i, y_i, σ_i) of a rescaled Laplacian of Gaussian
502 (LoG) function

503

$$L(x, y, \sigma) = \sigma^2 (\Delta(g_\sigma * f))(x, y, \sigma),$$

504

where $f_t(x, y)$ is the nuclei gray-scale value at time t , $g_\sigma(x, y)$ is Gaussian
505 kernel of width σ , and “ $g * f$ ” stands for the convolution of function g and f .

506

When multiple blobs were detected in a single nucleus, we deleted a
507 neighboring blob b_2 of b_1 with a heuristic test function T

508

$$T(b_1, b_2) = \frac{1}{2(f_t(b_1) + f_t(b_2))} - \int_r f_t(x) e^{-(x-\frac{1}{2})^2} dx,$$

509

where $\gamma : [0, 1] \rightarrow \mathbb{R}^2$ is the straight line from b_1 of b_2 .

510

511 We tracked the nuclei across frames based on a proximity criterion. The
512 distance between nucleus k in frame i and l in frame $i + 1$ was defined as

513
$$d_{k,l} = \| x_{k,i} - x_{l,i+1} \|_2.$$

514 We determined the interval of mitosis time using the k -means-clustering
515 algorithm on the observed nucleus positions at time t . If a new blob was
516 detected, we considered this nucleus and its nearest neighbor were daughter
517 nuclei from a recent mitosis, and set their internal nucleus clock to 0.

518 Calculations of nuclear displacement, speed, nuclear density, spindle length
519 and orientation were done for each nucleus in its own eigentime after mitosis.

520

521 **Laser ablation**

522 Stage embryos expressing Histone2Av-GFP and Cherry-Tubulin were used.
523 Cross-section images were recorded in the Cherry channel with a frame rate
524 of 1/s on a spinning disc microscope (100x/oil, NA1.4) with a CCD camera.
525 Spindle apparatus was ablated at spindle midzone by a line of 355 nm YAG
526 laser (DPSL-355/14, Rapp Opto Electronic) with the 15% of laser power, and
527 around 400 ms exposure time during the recording mode (100x oil, NA 1.4)
528 (Fig. S5).

529

530 **Particle Imaging Velocimetry (PIV) analyses**

531 Particle Imaging Velocimetry (PIV) of Histone2Av-GFP images (in Fig. S3, S7)
532 analysis was performed using square interrogation windows of side 16 pixels
533 with an overlap of 10 s “PIVlab” in MATLAB.

534

535 **Quantification of F-actin over cell cycle**

536 Embryos expressing Histone2Av-RFP; Utrophin-GFP were imaged with a
537 Zeiss LSM780 confocal microscope (25x/NA0.7 multi immersion). The frame
538 rate was 0.1 Hz, and 10 μm was covered in z direction. Utrophin-GFP stacks
539 were merged by average intensity projection (Fiji/ImageJ). F-actin was
540 quantified manually with Fiji/ImageJ.

541

542 **“Limited area” simulation of synchronous mitosis**

543 In the simulation, the nuclei are randomly placed in a 50 μm *50 μm square via
544 Poisson-disc sampling, which produces random tightly-packed locations with
545 pair-wise distances not smaller than a specified value $d_{\text{disc}} > 4\mu\text{m}$. We assume
546 the nuclei divide simultaneously and form mitotic spindles with isotropic
547 orientations. As the spindles extend with a constant speed, we check at each
548 time step if any two of the spindles touch each other by scanning a restricted
549 area of 4 μm *4 μm in the vicinity of each spindle (see supplementary video). If
550 a spindle touches at least one other, we assume it stops extending and
551 reaches its maximal length due to limited space. When all spindles reach their

552 respective maximal lengths, the simulation is ended and we compute the
553 average maximal length l_{\max} over all spindles in the simulation. For each fixed
554 d_{disc} , we run the simulation 50 times, producing 50 l_{\max} values for various
555 nuclear density around $1/(4d_{\text{disc}}^2)$. The mean of the 50 l_{\max} values and the
556 mean of the 50 nuclear densities provide the coordinates of one point in
557 Fig.5E. The x- and y- error bars indicate the respective standard deviations.
558 Varying the minimum distance d_{disc} between nuclei, we obtain the mean l_{\max}
559 values for a range of nuclear densities. The data from simulation are fitted to a
560 power-law function (solid curve in Fig. 5E) with the method of least squares.
561

562 **Computational modeling of the nuclear movement**

563 We extend the model by Kaiser, et al [15], which has previously been
564 successful in modeling static nuclei ordering during interphase, to now
565 account for nuclei dynamics during mitosis also now incorporating the
566 spherical topology of the embryo: Nuclei, positioned at \vec{r}_i , move due to
567 active forces, $\vec{F}_{act,ij}$, exerted by motor-activated pushing apart of overlapping

568 microtubule asters, and due to passive repulsive, $\vec{F}_{pass,ij}$, arising from the
569 visco-elastic matrix embedding the nuclei, built mainly from cytoskeletal actin.

570 The overdamped equation of motion is given by $\dot{\vec{r}}_i = \frac{1}{\eta} \sum_{j \neq i} (\vec{F}_{act,ij} + \vec{F}_{pass,ij})$,

571 where $\eta = 6\pi a\mu \approx 56 \times 10^{-6} \text{N m}^{-1} \text{s}^{-1}$ denotes the effective drag coefficient
572 for the approximately circular nuclei [42], where $a \approx 3 \mu\text{m}$ is the nuclear
573 radius and $\mu \approx 1 \text{Pa}$ is the viscosity of the matrix [22,23]. Both forces decay in
574 space following $1/r^4$. For the active force, this is justified because the
575 maximal force a single microtubule can exert scales like $1/r^2$ and the
576 density of microtubuli decays with $1/r^2$ in two dimensions. For a detailed
577 justification on the passive force, see Kaiser, et al [15].

578 The time dependence of the forces results from time dependent individual force
579 amplitudes contributed by each nucleus. In detail, forces are given by $\vec{F}_{pass,ij} =$

580 $-A_{pass}(t_i)A_{pass}(t_j) \frac{\vec{e}_{r_{i,j}}}{r_{i,j}^4}$ and $\vec{F}_{act,ij} = -A_{act}(t_i)A_{act}(t_j) \frac{\vec{e}_{r_{i,j}}}{r_{i,j}^4}$, where $\vec{e}_{r_{i,j}}$ and

581 $r_{i,j}$ denote the unit vector and the distance between nuclei i, j , respectively.
582 Nuclei divide when their age reaches $t_i = t_{\text{div}}$, and ages are initialized as $t_i =$

583 $t_{\text{div}} - \frac{2}{\pi} \theta_i t_{\text{wave}} - t_{\text{offset}}$, where θ_i is the polar coordinate of nucleus i . This

584 initialization leads to the division wave. For numerical stability, upon division,
585 the two daughter nuclei are placed a short distance r_{div} apart with random
586 orientation, their center of mass coinciding with the position of their mother.
587

588 To capture the dynamics of cytoskeletal elements during mitosis we subdivided
 589 the time course of events into the series: $t_{\text{spindle ass}} < t_{\text{spindle const}} < t_{\text{div}} <$
 590 $t_{\text{sp diss}} < t_{\text{MT ass}} < t_{\text{actin ass}} < t_{\text{MT inter}} < t_{\text{actin inter}}$. Passive forces change only
 591 between $t_{\text{spindle ass}} < t_{\text{spindle const}}$ when actin caps shrink while spindles
 592 assemble generating balancing forces and during regrowth of actin caps
 593 between $t_{\text{actin ass}} < t_{\text{actin inter}}$ before entering interphase. Active forces in
 594 contrast are much more dynamic: Between $t_{\text{spindle ass}} < t_{\text{spindle const}}$ spindles
 595 assemble and the active force grows to exert a maximal force of h_{spindle} . After
 596 division $t_{\text{div}} < t_{\text{spindle diss}}$ spindles move daughter nuclei apart: The active force
 597 between the division partners is now increased by an additional time-dependent

598 factor A_{div} that reaches values of up to 3, $\vec{F}_{\text{act},i,i+1} =$

599 $-A_{\text{div}}(t)A_{\text{act}}(t)A_{\text{act}}(t)\frac{\vec{e}_{r_{i,i+1}}}{r_{i,i+1}^4}$, where t is the common time of both daughter

600 nuclei. After $t_{\text{spindle diss}}$, forces between paired daughter nuclei reduce linearly
 601 to regular levels. Meanwhile, for all other nuclei, after division the active force
 602 is halved since each nucleus is only associated with one centrosome, instead
 603 of two as before. This is balanced by the effective increase of passive forces
 604 as nuclei are closer packed due to division while the passive force amplitude
 605 stays constant. Between $t_{\text{spindle diss}} < t_{\text{MT ass}}$ spindles disassemble before the
 606 microtubule asters regrow during $t_{\text{MT ass}} < t_{\text{MT inter}}$. All dynamics are
 607 interpolated linearly. In detail:

608 $A_{\text{pass}}(t) =$

$$609 \left\{ \begin{array}{ll} h_{\text{inter}} & t \leq t_{\text{spindle ass}} \\ h_{\text{inter}} + (h_{\text{mitosis}} - h_{\text{inter}}) \frac{t - t_{\text{spindle ass}}}{t_{\text{spindle const}} - t_{\text{spindle ass}}} & t_{\text{spindle ass}} \leq t \leq t_{\text{spindle const}} \\ h_{\text{mitosis}} & t_{\text{spindle const}} \leq t \leq t_{\text{actin ass}} \\ h_{\text{mitosis}} + (h_{\text{inter}} - h_{\text{mitosis}}) \frac{t - t_{\text{actin ass}}}{t_{\text{actin inter}} - t_{\text{actin ass}}} & t_{\text{actin ass}} \leq t \leq t_{\text{actin inter}} \\ h_{\text{inter}} & t_{\text{actin inter}} \leq t \end{array} \right. ,$$

610 $A_{\text{act}}(t) =$

$$611 \left\{ \begin{array}{ll} h_{\text{MT}} & t \leq t_{\text{spindle ass}} \\ h_{\text{MT}} + (h_{\text{sp}} - h_{\text{MT}}) \frac{t - t_{\text{spindle ass}}}{t_{\text{spindle const}} - t_{\text{spindle ass}}} & t_{\text{spindle ass}} \leq t \leq t_{\text{spindle const}} \\ h_{\text{spindle}} & t_{\text{spindle const}} \leq t \leq t_{\text{div}} \\ \frac{1}{2} h_{\text{spindle}} & t_{\text{div}} \leq t \leq t_{\text{spindle diss}} \\ \frac{1}{2} h_{\text{spindle}} + \frac{1}{2} (h_{\text{spindle diss}} - h_{\text{spindle}}) \frac{t - t_{\text{spindle diss}}}{t_{\text{MT ass}} - t_{\text{spindle diss}}} & t_{\text{spindle diss}} \leq t \leq t_{\text{MT ass}} \\ \frac{1}{2} h_{\text{spindle diss}} + \frac{1}{2} (h_{\text{MT}} - h_{\text{spindle diss}}) \frac{t - t_{\text{MT ass}}}{t_{\text{MT inter}} - t_{\text{MT ass}}} & t_{\text{MT ass}} \leq t \leq t_{\text{MT inter}} \\ \frac{1}{2} h_{\text{MT}} & t_{\text{MT inter}} \leq t \end{array} \right. ,$$

$$A_{\text{div}}(t) = \begin{cases} h_{\text{div}} \frac{t - t_{\text{div}}}{t_{\text{spindle diss}}/2 - t_{\text{div}}} & t_{\text{div}} \leq t \leq t_{\text{spindle diss}}/2 \\ h_{\text{div}} & t_{\text{spindle diss}}/2 \leq t \leq t_{\text{spindle diss}} \\ h_{\text{div}} - (h_{\text{div}} - 1) \frac{t - t_{\text{spindle diss}}}{t_{\text{MT ass}} - t_{\text{spindle diss}}} & t_{\text{spindle diss}} \leq t \leq t_{\text{MT ass}} \\ 1 & t_{\text{MT ass}} \leq t \end{cases}$$

613

614 Note that changes in both passive and active forces only get out of balance -
 615 initiating nuclei motion - during spindle disassembly with significant time delay
 616 relative to the time point of nuclei division. At that point in time nuclei that have
 617 not divided yet exert a stronger repulsive force than the already divided nuclei,
 618 since their actin caps and microtubule asters are not fully reformed. Therefore,
 619 nuclei move toward the region of higher nuclei density, only returning back
 620 when actin caps and microtubule asters are forming again.

621

622 Choices for the model parameters are found in the table below. Their
 623 magnitudes are chosen to match the length of the cell cycle, 800s, and the
 624 maximal force exerted by a single microtubule, which is around 3pN according
 625 to [43]. In total, the forces on a single nucleus range between 10-100pN, the
 626 same order of magnitude as the force applied to a single magnetic microparticle
 627 by [24] to move it through the cellularizing tissue in an early drosophila embryo.
 628 Note that computing the force involves multiplying the two amplitudes and
 629 dividing by the distance to the power of four.

630

$t_{\text{spindle ass}}$	$t_{\text{spindle const}}$	t_{div}	$t_{\text{sp diss}}$	$t_{\text{MT ass}}$	$t_{\text{actin ass}}$	$t_{\text{MT inter}}$	$t_{\text{actin inter}}$
-200s	-80s	0s	70s	200s	240s	400s	600s

631

632

h_{inter}	h_{mitosis}	h_{MT}	h_{spindle}	$h_{\text{spindle diss}}$	h_{div}
$4e-17 \text{ N}^{1/2} \text{ m}^2$	$1e-17 \text{ N}^{1/2} \text{ m}^2$	$4e-17 \text{ N}^{1/2} \text{ m}^2$	$8e-16 \text{ N}^{1/2} \text{ m}^2$	$0 \text{ N}^{1/2} \text{ m}^2$	3

633

634

635 Spring constant fitting

636 The data sets consisted of 1–5 nuclear displacement curves for 2–4 embryos
 637 of each type (*dia*, *ELMO*, *Kinesin5* and *Map60* mutants, wild type).

638 The nuclear displacement curves (in the first phase) are similar to the
 639 oscillation of a not-actively driven and non-damped harmonic oscillator.

640 Therefore, the individual nuclear displacement curves were fitted to a sine
 641 curve of the form $y(t) = A \sin(\omega t + \varphi)$,

642 where A is the amplitude, ω the angular frequency and φ the phase shift,

643 using a self-written script in Python. The biological rationale behind this

644 approach is that the nuclei behave like they were linked to an elastic spring,

645 which could be e.g. linkages to the cytoskeleton. At $t=0$ the spring is stretched
646 and the nuclei start to move until the spring is compressed and the nuclei
647 move back.

648

649 The fit region was determined as follows. For all curves, the lower bound on
650 the fitting range was set equal to the point in time where the nuclear
651 displacement first exceeds $5\ \mu\text{m}$, as some curves show a small, reversible
652 displacement in the beginning. The upper bound was chosen independently
653 for each of the data sets since the elastic part of the curve depends on the
654 stiffness and dampening of the spring and hence differs across data sets. For
655 the *dia* and *Map60* mutants as well as the wild type, the upper bound was set
656 equal to 100 s after the turning point, while it was set to 180 s after for the
657 *ELMO* mutant and 240 s for the Kinesin5 mutants. The results of the fit
658 parameter ω were averaged for each embryo to give a set of angular
659 frequencies ω_i for each type, where i runs over the number of embryos. The
660 spring constant was derived from the average ω_i via the relation
661 $k = m (\omega_i)^2$, in which m denotes the mass of the nucleus. It was assumed that
662 the nuclei are spherical with a diameter of $4.9\ \mu\text{m}$ and a density equal to that
663 of water at room temperature. Error bars, which correspond to one standard
664 deviation, were calculated in the frequency domain and then converted to the
665 force domain by the analogue of the relation above.

666

667 **Acknowledgements**

668 We are grateful to D. Görlich, T. Lecuit, B. Loppin and the members of the
669 Grosshans laboratory for stains, materials and discussions. We acknowledge
670 service support from the Bloomington Drosophila Stock Center (supported by
671 NIH P40OD018537). X.Z. was supported by Center for Advancing Electronics
672 Dresden (cfaed) and by the Deutsche Forschungsgemeinschaft (DFG,
673 German Research Foundation) under Germany's Excellence Strategy – EXC-
674 2068 – 390729961– Cluster of Excellence Physics of Life of TU Dresden. This
675 work was in part supported by the Göttingen Centre for Molecular Biology
676 (funds for equipment repair) and the Deutsche Forschungsgemeinschaft
677 (DFG, SFB-937/A10, SFB-937/A19 and equipment grant INST1525/16-1
678 FUGG).

679

680 **Author contributions**

681 ZL and DK conducted the experiments. ZL, JR, HP, SK analyzed the data.
682 SM, XZ, KA conducted the simulations. JG and ZL conceived and JG, TA,
683 SG, KA supervised the study. JG, ZL and XZ wrote the manuscript.

684

685 **References:**

686 [1] Couzin ID. Synchronization: The Key to Effective Communication in

- 687 Animal Collectives. *Trends in Cognitive Sciences* 2018;22:844–6.
688 doi:10.1016/j.tics.2018.08.001.
- 689 [2] Partridge BL. Rigid definitions of schooling behaviour are inadequate.
690 *Animal Behaviour* 1982;30:298–9.
- 691 [3] Moussaid M, Garnier S, Theraulaz G, Helbing D. Collective
692 Information Processing and Pattern Formation in Swarms, Flocks, and
693 Crowds. *Topics in Cognitive Science* 2009;1:469–97.
694 doi:10.1111/j.1756-8765.2009.01028.x.
- 695 [4] Chialvo DR. Emergent complex neural dynamics. *Nature Physics*
696 2010;6:744–50. doi:10.1038/nphys1803.
- 697 [5] Levina A, Herrmann JM, Geisel T. Dynamical synapses causing self-
698 organized criticality in neural networks. *Nature Physics* 2007;3:857–
699 60. doi:10.1038/nphys758.
- 700 [6] Plenz D, Thiagarajan TC. The organizing principles of neuronal
701 avalanches: cell assemblies in the cortex? *Trends in Neurosciences*
702 2007;30:101–10. doi:10.1016/j.tins.2007.01.005.
- 703 [7] McMahan A, Supatto W, Fraser SE, Stathopoulos A. Dynamic
704 Analyses of *Drosophila* Gastrulation Provide Insights into Collective
705 Cell Migration. *Science* 2008;322:1546–50.
706 doi:10.1126/science.1167094.
- 707 [8] Farrell JA, Wang Y, Riesenfeld SJ, Shekhar K, Regev A, Schier AF.
708 Single-cell reconstruction of developmental trajectories during
709 zebrafish embryogenesis. *Science* 2018;360:eaar3131.
710 doi:10.1126/science.aar3131.
- 711 [9] Sumino Y, Nagai KH, Shitaka Y, Tanaka D, Yoshikawa K, Chaté H, et
712 al. Large-scale vortex lattice emerging from collectively moving
713 microtubules. *Nature* 2012;483:448–52. doi:10.1038/nature10874.
- 714 [10] Schaller V, Weber C, Semmrich C, Frey E, Bausch AR. Polar patterns
715 of driven filaments. *Nature* 2010;467:73–7. doi:10.1038/nature09312.
- 716 [11] Butt T, Mufti T, Humayun A, Rosenthal PB, Khan S, Khan S, et al.
717 Myosin motors drive long range alignment of actin filaments. *The*
718 *Journal of Biological Chemistry* 2010;285:4964–74.
719 doi:10.1074/jbc.M109.044792.
- 720 [12] Deneke VE, Melbinger A, Vergassola M, Di Talia S. Waves of Cdk1
721 Activity in S Phase Synchronize the Cell Cycle in *Drosophila* Embryos.
722 *Developmental Cell* 2016;38:399–412.
723 doi:10.1016/j.devcel.2016.07.023.
- 724 [13] Idema T, Dubuis JO, Kang L, Manning ML, Nelson PC, Lubensky TC,
725 et al. The Syncytial *Drosophila* Embryo as a Mechanically Excitable
726 Medium. *PLoS ONE* 2013;8:e77216.
727 doi:10.1371/journal.pone.0077216.
- 728 [14] Kanasaki T, Edwards CM, Schwarz US, Grosshans J. Dynamic

- 729 ordering of nuclei in syncytial embryos: a quantitative analysis of the
730 role of cytoskeletal networks. *Integrative Biology (Camb)*
731 2011;3:1112–9. doi:10.1039/c1ib00059d.
- 732 [15] Kaiser F, Lv Z, Marques Rodrigues D, Rosenbaum J, Aspelmeier T,
733 Grosshans J, et al. Mechanical Model of Nuclei Ordering in *Drosophila*
734 Embryos Reveals Dilution of Stochastic Forces. *Biophysical Journal*
735 2018;114:1730–40. doi:10.1016/j.bpj.2018.02.018.
- 736 [16] Quinlan ME. Cytoplasmic Streaming in the *Drosophila* Oocyte. *Annual*
737 *Review of Cell and Developmental* 2016;32:173–95.
738 doi:10.1146/annurev-cellbio-111315-125416.
- 739 [17] Woodhouse FG, Goldstein RE. Cytoplasmic streaming in plant cells
740 emerges naturally by microfilament self-organization. *Proceedings of*
741 *the National Academy of Sciences of the United States of America*
742 2013;110:14132–7. doi:10.1073/pnas.1302736110.
- 743 [18] Shimmen T, Yokota E. Cytoplasmic streaming in plants. *Current*
744 *Opinion in Cell Biology* 2004;16:68–72.
745 doi:10.1016/j.ceb.2003.11.009.
- 746 [19] Deneke VE, Puliafito A, Krueger D, Narla AV, De Simone A, Primo L,
747 et al. Self-Organized Nuclear Positioning Synchronizes the Cell Cycle
748 in *Drosophila* Embryos. *Cell* 2019. doi:10.1016/j.cell.2019.03.007.
- 749 [20] He B, Doubrovinski K, Polyakov O, Wieschaus E. Apical constriction
750 drives tissue-scale hydrodynamic flow to mediate cell elongation.
751 *Nature* 2014;508:392–6. doi:10.1038/nature13070.
- 752 [21] Winkler F, Gummalla M, Künneke L, Lv Z, Zippelius A, Aspelmeier T,
753 et al. Fluctuation Analysis of Centrosomes Reveals a Cortical Function
754 of Kinesin-1. *Biophysical Journal* 2015;109:856–68.
755 doi:10.1016/j.bpj.2015.07.044.
- 756 [22] Wessel AD, Gumalla M, Grosshans J, Schmidt CF. The mechanical
757 properties of early *Drosophila* embryos measured by high-speed video
758 microrheology. *Biophysical Journal* 2015;108:1899–907.
759 doi:10.1016/j.bpj.2015.02.032.
- 760 [23] Doubrovinski K, Swan M, Polyakov O, Wieschaus EF. Measurement
761 of cortical elasticity in *Drosophila melanogaster* embryos using
762 ferrofluids. *Proceedings of the National Academy of Sciences of the*
763 *United States of America* 2017;114:1051–6.
764 doi:10.1073/pnas.1616659114.
- 765 [24] D’Angelo A, Dierkes K, Carolis C, Salbreux G, Solon J. In Vivo Force
766 Application Reveals a Fast Tissue Softening and External Friction
767 Increase during Early Embryogenesis. *Current Biology* 2019;29:1564–
768 6. doi:10.1016/j.cub.2019.04.010.
- 769 [25] Vergassola M, Deneke VE, Di Talia S. Mitotic waves in the early
770 embryogenesis of *Drosophila*: Bistability traded for speed.

- 771 Proceedings of the National Academy of Sciences of the United States
772 of America 2018;115:E2165–74. doi:10.1073/pnas.1714873115.
- 773 [26] Scholey JM. Kinesin-5 in *Drosophila* embryo mitosis: Sliding filament
774 or spindle matrix mechanism? *Cell Motility and the Cytoskeleton*
775 2009;66:500–9. doi:10.1002/cm.20349.
- 776 [27] Roseboom AJ, Aspelmeier J, Grosshans J. A “molecular
777 guillotine” reveals an interphase function of Kinesin-5. *Journal of Cell*
778 *Science* 2018;jcs.210583. doi:10.1242/jcs.210583.
- 779 [28] Sullivan W, Theurkauf WE. The cytoskeleton and morphogenesis of
780 the early *Drosophila* embryo. *Current Opinion in Cell Biology*
781 1995;7:18–22. doi:10.1016/0955-0674(95)80040-9.
- 782 [29] Karr TL, Alberts BM. Organization of the cytoskeleton in early
783 *Drosophila* embryos. *The Journal of Cell Biology* 1986;102:1494–509.
784 doi:10.1083/jcb.102.4.1494.
- 785 [30] Rauzi M, Lenne P-F, Lecuit T. Planar polarized actomyosin contractile
786 flows control epithelial junction remodelling. *Nature* 2010;468:1110–4.
787 doi:10.1038/nature09566.
- 788 [31] Schmidt A, Lv Z, Grosshans J. ELMO and Sponge specify subapical
789 restriction of Canoe and formation of the subapical domain in
790 early *Drosophila* embryos. *Development* 2018;145:dev157909.
791 doi:10.1242/dev.157909.
- 792 [32] Geisbrecht ER, Haralalka S, Swanson SK, Florens L, Washburn MP,
793 Abmayr SM. *Drosophila* ELMO/CED-12 interacts with Myoblast city to
794 direct myoblast fusion and ommatidial organization. *Developmental*
795 *Biology* 2008;314:137–49. doi:10.1016/j.ydbio.2007.11.022.
- 796 [33] Afshar K, Stuart B, Wasserman SA. Functional analysis of the
797 *Drosophila* diaphanous FH protein in early embryonic development.
798 *Development* 2000;127:1887–97. doi:10.1083/jcb.137.1.169.
- 799 [34] Grosshans J, Wenzl C, Herz H-M, Bartoszewski S, Schnorrer F, Vogt
800 N, et al. RhoGEF2 and the formin Dia control the formation of the
801 furrow canal by directed actin assembly during *Drosophila*
802 cellularisation. *Development* 2005;132:1009–20.
803 doi:10.1242/dev.01669.
- 804 [35] Wenzl C, Yan S, Laupsien P, Grosshans J. Localization of RhoGEF2
805 during *Drosophila* cellularization is developmentally controlled by
806 Slam. *Mechanisms of Development* 2010;127:371–84.
807 doi:10.1016/j.mod.2010.01.001.
- 808 [36] Blythe SA, Wieschaus EF. Zygotic genome activation triggers the DNA
809 replication checkpoint at the midblastula transition. *Cell*
810 2015;160:1169–81. doi:10.1016/j.cell.2015.01.050.
- 811 [37] Benton MA, Akam M, Pavlopoulos A. Cell and tissue dynamics during
812 *Tribolium* embryogenesis revealed by versatile fluorescence labeling

- 813 approaches. *Development* 2013;140:3210–20.
814 doi:10.1242/dev.096271.
- 815 [38] Gramates LS, Marygold SJ, Santos GD, Urbano J-M, Antonazzo G,
816 Matthews BB, et al. FlyBase at 25: looking to the future. *Nucleic Acids*
817 *Research* 2017;45:D663–71. doi:10.1093/nar/gkw1016.
- 818 [39] Cook KR, Parks AL, Jacobus LM, Kaufman TC, Matthews K. New
819 research resources at the Bloomington Drosophila Stock Center. *Fly*
820 2010;4:88–91. doi:10.4161/fly.4.1.11230.
- 821 [40] Loppin B, Docquier M, Bonneton F, Couble P. The Maternal Effect
822 Mutation *sésame* Affects the Formation of the Male Pronucleus in
823 *Drosophila melanogaster*. *Developmental Biology* 2000;222:392–404.
824 doi:10.1006/dbio.2000.9718.
- 825 [41] Schindelin J, Arganda-Carreras I, Frise E, Kaynig V, Longair M,
826 Pietzsch T, et al. Fiji: an open-source platform for biological-image
827 analysis. *Nature Methods* 2012;9:676–82. doi:10.1038/nmeth.2019.
- 828 [42] Koke C, Kanesaki T, Grosshans J, Schwarz US, Dunlop CM. A
829 computational model of nuclear self-organisation in syncytial embryos.
830 *Journal of Theoretical Biology* 2014;359:92–100.
831 doi:10.1016/j.jtbi.2014.06.001.
- 832 [43] Vleugel M, Kok M, Dogterom M. Understanding force-generating
833 microtubule systems through in vitro reconstitution. *Cell Adhesion and*
834 *Migration* 2016;10:475–94. doi:10.1080/19336918.2016.1241923.
835

836 **Figure 1. Quantitative assay for nuclear movement.**

837 (A), Live image of an embryo during mitosis. The left half is in metaphase, the
838 right half in anaphase. The dotted line in red indicates metaphase-anaphase
839 transition sweeping over the embryo from right to left as a wave front.
840 (B), Snapshots show the nuclear motion. The red line indicates the
841 metaphase-anaphase transition. Blue line is the forward trajectories of nuclei.
842 The right panel is the corresponding angle distribution of nuclear motion.
843 (C), The projection of the nuclear motion. Red arrow indicates the nuclear
844 division.
845 (D, E), Time course of nuclear displacement with the position of the mother
846 nucleus and nuclear speeds during metaphase-anaphase transition as a
847 reference ($t=0$) ($n=260$ nuclei in one embryo, representative for all embryos
848 which have been checked). The numbers indicate ① chromosome
849 segregation, ② forth movement away and ③ back movement toward the
850 mitotic wave front. The right panel is a snapshot of nuclear movement labelled
851 with three numbers. The image is the end of the nuclear movement.
852 (F), The maximal displacement plotted against the corresponding speed of the
853 mitotic wave ($n=50$ embryos).

854

855 **Figure 2. Emergence of collective nuclear movement.**

856 (A), Schematic drawing of an embryo with definition of angles.
857 (B), Image from live imaging after mitosis. Orientations of the corresponding
858 spindle at $t=0$ s and the directions of nuclear movement at $t = 60$ s are
859 indicated by a magenta bar and green arrow, respectively.
860 (C), Distribution of observed angles for spindle orientation at $t=0$ s and
861 nuclear movement at $t=60$ s. ($n=20$ embryos including 6230 nuclei).
862 (D), Image series with previous trajectories showing cases of perpendicular
863 and parallel mitosis.
864 (E), Time course of nuclear displacement (blue) and distance between
865 corresponding daughter nuclei (orange). The time lag (τ) between maxima is
866 indicated ($n=260$ nuclei in one embryo, representative for all embryos we
867 have checked).
868 (F), Distribution of the time lag (τ) ($n=21$ embryos).
869 (G), The schematic drawing of the transition from individual movement to
870 collective behavior. Data are mean \pm s.e.m. Scale bar: 10 μ m

871

872 **Figure 3. Numerical simulation of nuclear movement.**

873 (A), Scheme of division, active and passive forces in syncytial embryo.
874 (B), Snapshots from the simulation. Nuclei were projections. Color code
875 indicates speed of nuclear movement.
876 (C), Time course of nuclear displacement ($n=300$ nuclei).

877 (D), Time course of nuclear displacement (blue) and distance between
878 corresponding daughter nuclei (orange) (n=300 nuclei). The time lag (τ)
879 between maxima is indicated.
880 (E), Distribution of the time lag (τ) (n=21 embryos).
881 (F), The negative correlation between maximal displacement and the
882 corresponding speed of the mitotic wave.
883 (G), Time course of nuclear displacement in wave (wild type) embryo and
884 “salt-and-pepper pattern” embryo (n=300 nuclei in both cases, respectively).
885 (H), The positive correlation between maximal displacement and division
886 distance. Data are mean \pm s.e.m.

887

888 **Figure 4. Forces mediating Yo-Yo movement of nuclei *in vivo*.**

889 (A). Spindle length/distance between respective daughter nuclei in embryos
890 partially depleted of Kinesin-5 and *Map60* mutants (n=30 spindle in 3 embryos
891 for each genotype).
892 (B), Images from live image. The trajectories of two nuclei over 300 s were
893 plotted into the images. Images were the end of the movement.
894 (C), Time course of nuclear displacement.
895 (D), Maximal displacement was plotted against corresponding division
896 distance. (n=290 nuclei in wild type, 256 nuclei in *kin5*, 292 nuclei in *Map60* in
897 Fig. C and D).
898 (E), Scheme of cortical actin dynamics during nuclear division cycles.
899 (F), ELMO and Dia are involved in F-actin cortex formation.
900 (G), Images from movies of *dia* and *ELMO* mutants. Nuclear trajectories over
901 10 min are plotted into the images. Images were the end of the nuclear
902 movement.
903 (H, J), Time course of displacement in *ELMO* and *dia* mutants.
904 (J), The final distance between the current position and original position of the
905 nuclei after yo-yo movement, as indicated as “d” in H and I (n=260 nuclei in
906 wild type, 45 nuclei in *ELMO* mutant and 90 in *dia* mutant embryo in Fig. H, I,
907 J). The Data are mean \pm s.e.m. Scale bar: 10 μ m.

908

909 **Figure 5. Long mitotic spindles require pseudo-synchronous nuclear
910 cycles.**

911 (A), Live image series of the process of nuclear dividing.
912 (B), Quantification of the distance between splitting nuclear pair in cleavage
913 cycles.
914 (C) The protected area between daughter nuclei containing the spindle is
915 indicated by an overlaid colored area.
916 (D), Illustration of the simulation. Green dots indicate nuclei. Blue arrows
917 indicate spindles. Red dots indicate the touching of the neighbor spindles,
918 leading to the spindle growth stops.

919 (E), Spindle lengths/distances between daughter nuclei are plotted against the
920 corresponding nuclear density. Data from simulation (blue) and
921 measurements in embryos in NC11, NC12, NC13 in diploids and NC14 in
922 haploids (orange) (n=15 spindles in each embryo and 3 embryos for each
923 type).

924

925 **Figure S1. Characterization of nuclear dynamics in syncytial embryo.**

926 (A), Embryo to embryo variation of the speed of the wave front (n=50
927 embryos).

928 (B), Image series with Voronoi maps with the mitotic wave front in images at
929 35 s and 55 s. Color code indicates nuclear density.

930 (C), Time course of nuclear density with metaphase-anaphase transition at
931 t=0. Numbers indicate the three stages of nuclear movement. (n=260 nuclei in
932 one embryo).

933 (D). Schematic drawing shows nuclei move like an elastic sheet.

934 (E), A simple square function (red) was fitted to the forth and back movement
935 around the maximal displacement. According to Hook's law an apparent
936 spring constant ($1.5 \pm 0.02 \times 10^{-18} \text{ Nm}^{-1}$) was calculated (n=15 nuclei from 3
937 embryos). Data are mean \pm s.e.m. Scale bar: 10 μm .

938

939 **Figure S2. Nuclear displacement and flow speeds are less pronounced
940 in earlier cycles.**

941 (A), The time course of nuclear displacement in NC11, 12 and 13 in one
942 embryo (n=58, 107 and 206 nuclei in NC11, 12 and 13, respectively).

943 (B), Maximal displacement distribution in NC11, 12 and 13 from (A).

944 (C), Time course of nuclear flow speed from the same embryo as shown in a,
945 with colour-coding for indicated nuclear cycles.

946 (D), The percentage of embryos showing the nuclear movements ①, ② and
947 ③ in different cycles (n=6, 18, 26 embryos in NC11, 12 and 13, respectively).

948 Data are mean \pm s.e.m.

949

950 **Figure S3. The nuclei move as a sheet.**

951 (A), Groups of cells have been marked in color at metaphase. Their daughter
952 nuclei were labelled with the same color in the following images.

953 (B) Particle Imaging Velocimetry analysis show that the nuclei move
954 collectively like a sheet.

955

956 **Figure S4. The parameters for Numerical simulation used in Fig. 3.**

957 (A), Time course of the division, active force and passive force used in the
958 simulation.

959 (B), Increasing in spindle strength ($h_{spindle}$) leads to increasing of maximal
960 displacement and division distance. Data are mean \pm s.e.m.

961

962 **Figure S5. Laser cutting on spindle in metaphase.** The embryo expressing
963 mCherry-Tubulin was used for monitor the spindle structure. The spindle
964 recovers in second-scale after laser ablation.

965

966 **Figure S6. Actin cortex represses nuclear movement.**

967 (A), Live-images showing F-actin organization during nuclear cycle.

968 (B), Quantification of F-actin. (n=10 regions in 3 independent recordings).

969 (C, D), Injection of ROCK inhibitor Y-27632 leads to the reduction of nuclear
970 motion as well as spindle elongation.

971 (E, F), Time course of single nuclear displacement and the local myosin/F-
972 actin intensity.

973 (E), Fixed *dia* and *ELMO* mutants stained for F-actin (red) and DNA (blue).

974 (F), Maximal displacement and final distance of nuclear dynamics in *dia* and
975 *ELMO* mutants.

976 (G), Apparent spring constant.

977 (H), Images from movies of wild type and *ELMO* mutants in NC12. Nuclear
978 trajectories are plotted into the first images. (I), The time course of nuclear

979 displacement in NC12. (n=130 nuclei in *ELMO* and 290 nuclei in wild type.

980 Data are mean±s.e.m. Scale bar: 10 μm.

981

982 **Figure S7. Nuclei move as a sheet in *dia* and *ELMO* mutant embryo.**

983 (A), Snapshots from movies at indicated time. Groups of cells have been
984 marked in color at metaphase. Their daughter nuclei were labelled with the
985 same color in the following images.

986 (B). Particle Imaging Velocimetry analysis show that the nuclei move
987 collectively.

988

989 **Figure S8. Nuclear densities in different cycles.**

990 (A), Images of *Drosophila* syncytial embryo expressing Histone2Av-GFP in
991 different cycles.

992 (B), Quantification of nuclear density in the indicated cycles. n=10 embryos.
993 Data are mean±s.e.m.

994

995 **Figure S9. Daughter nuclei cannot separate in *nmk grp* and *mei41 zld***
996 **mutant embryos.**

997

998 **Figure S10. Mitotic wave speed in the indicated embryos.**

999

1000 **Figure S11. The asymmetric force field leads to the nuclear directional**
1001 **movement.**

1002 (A), The repulsive force between daughter nuclei increases in anaphase
1003 pushing the daughter nuclei apart, followed by a drop in telophase due to
1004 spindle disassembly.
1005 (B), The summing up of all nuclei in an embryo at a given mitotic time results
1006 in an asymmetric force field, which likely determines the directionality of the
1007 nuclear flow in telophase.
1008
1009 **Movie list:**
1010 Movie 1. Mitotic wave sweeps over the embryo.
1011
1012 Movie 2. Nuclei undergo stereotypical movement after metaphase-anaphase
1013 transition. Scale bar: 10 μm .
1014
1015 Movie 3. The time course of the nuclear Voronoi map over nuclear division.
1016 Scale bar: 10 μm .
1017
1018 Movie 4. Nuclei move as a laminar flow shown in PIV analysis. Scale bar: 10
1019 μm .
1020
1021 Movie 5. Computational simulation.
1022
1023 Movie 6. The nuclear displacement in wild type, dia and ELMO mutant
1024 embryos. Scale bar: 20 μm .
1025
1026

Figure 1

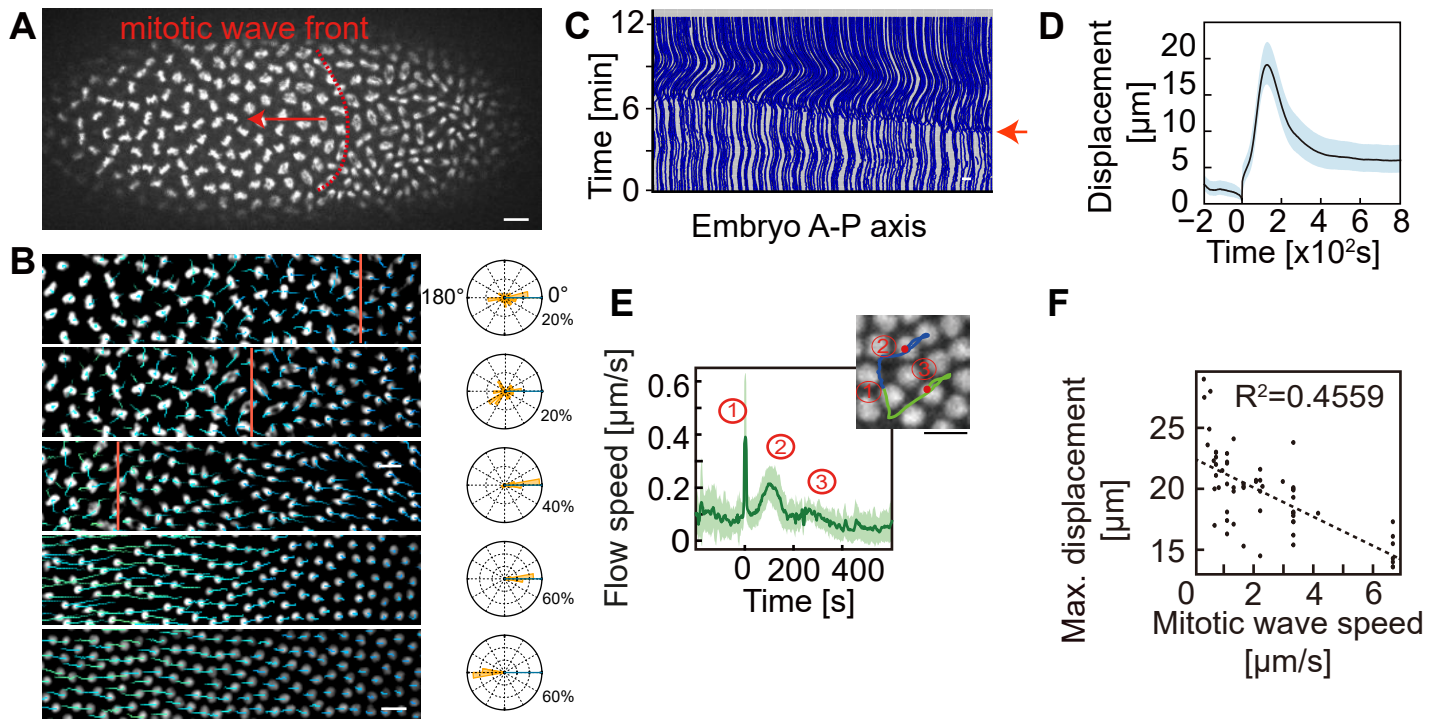


Figure 2

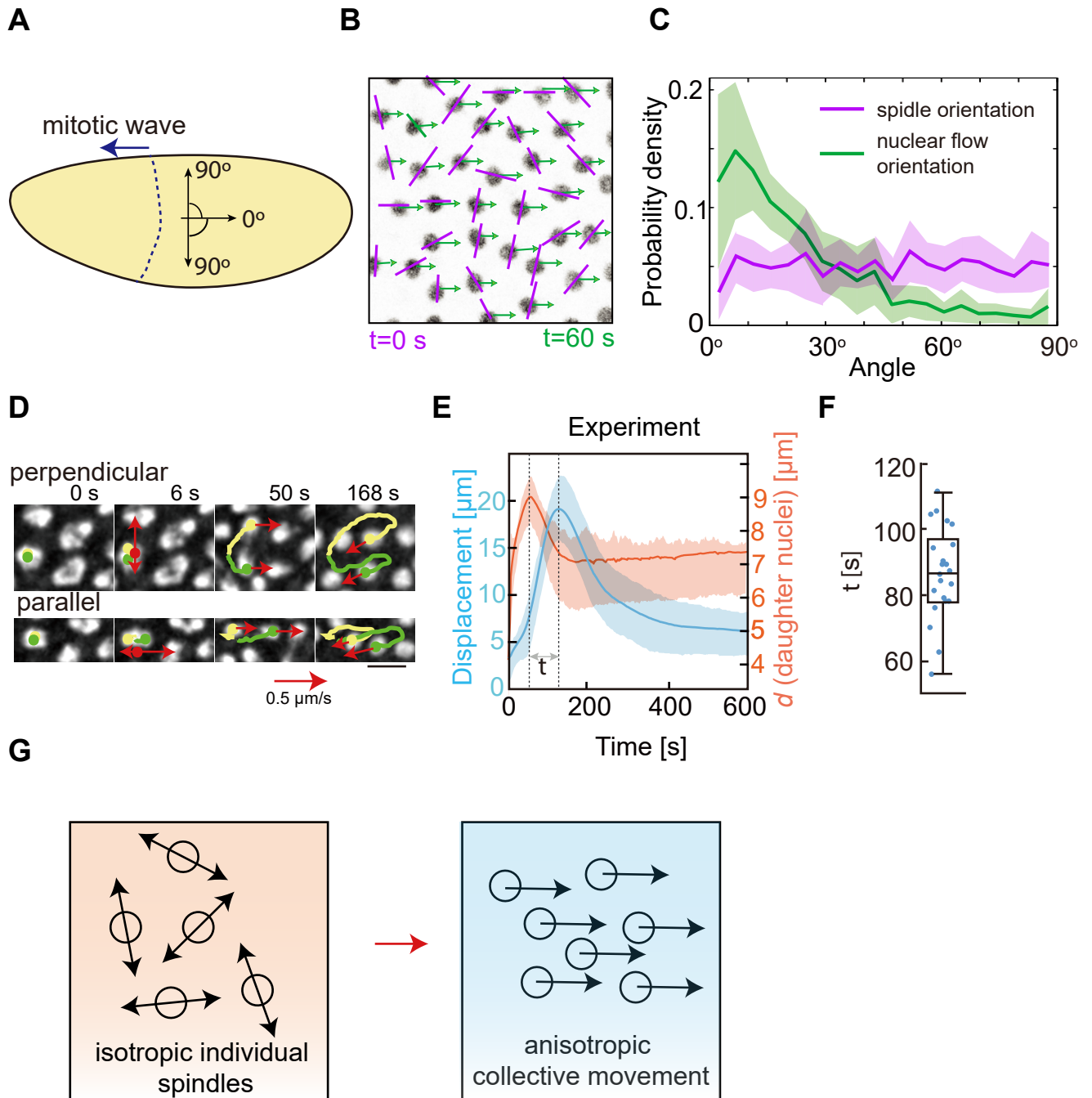


Figure 3

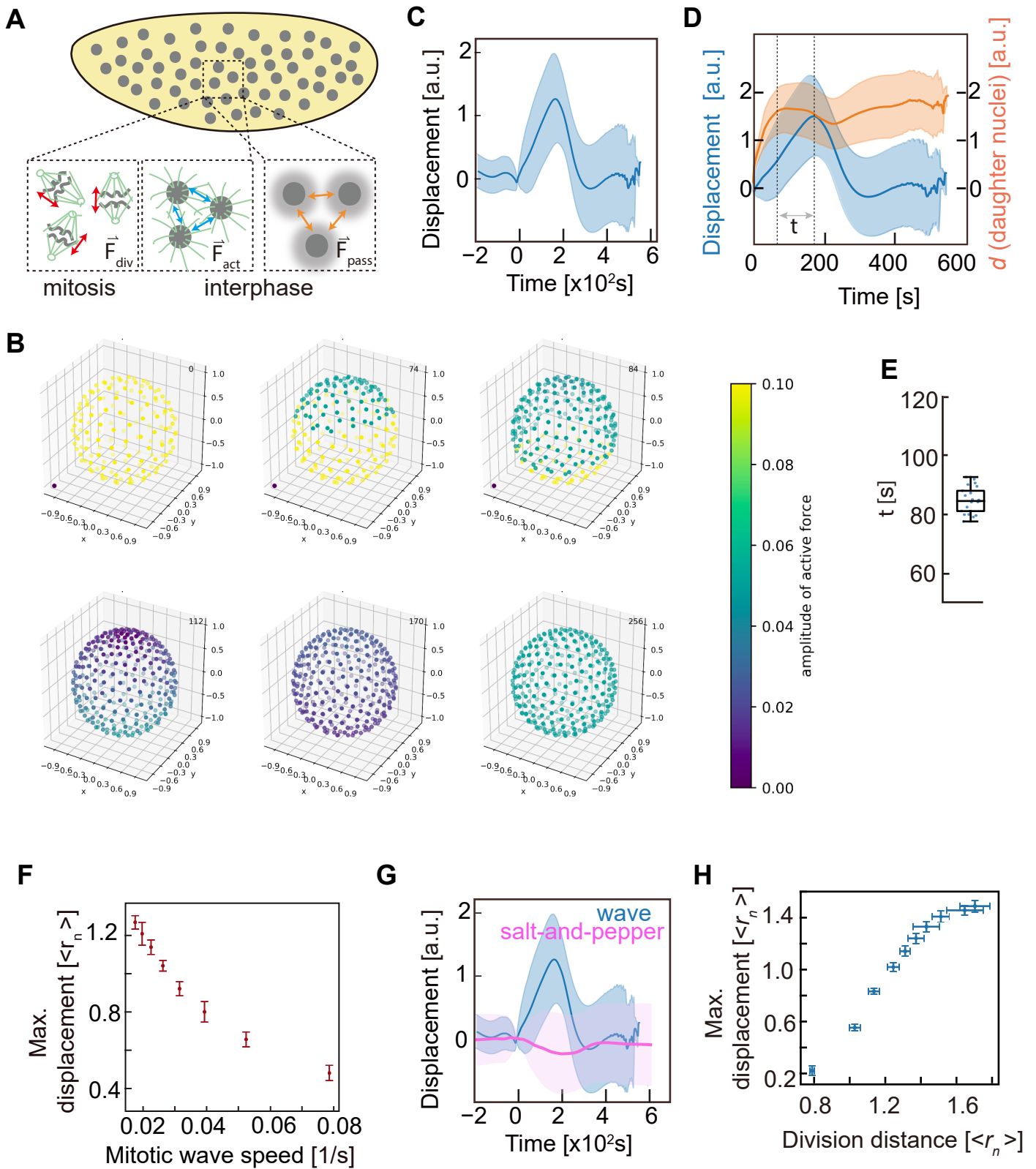


Figure 4

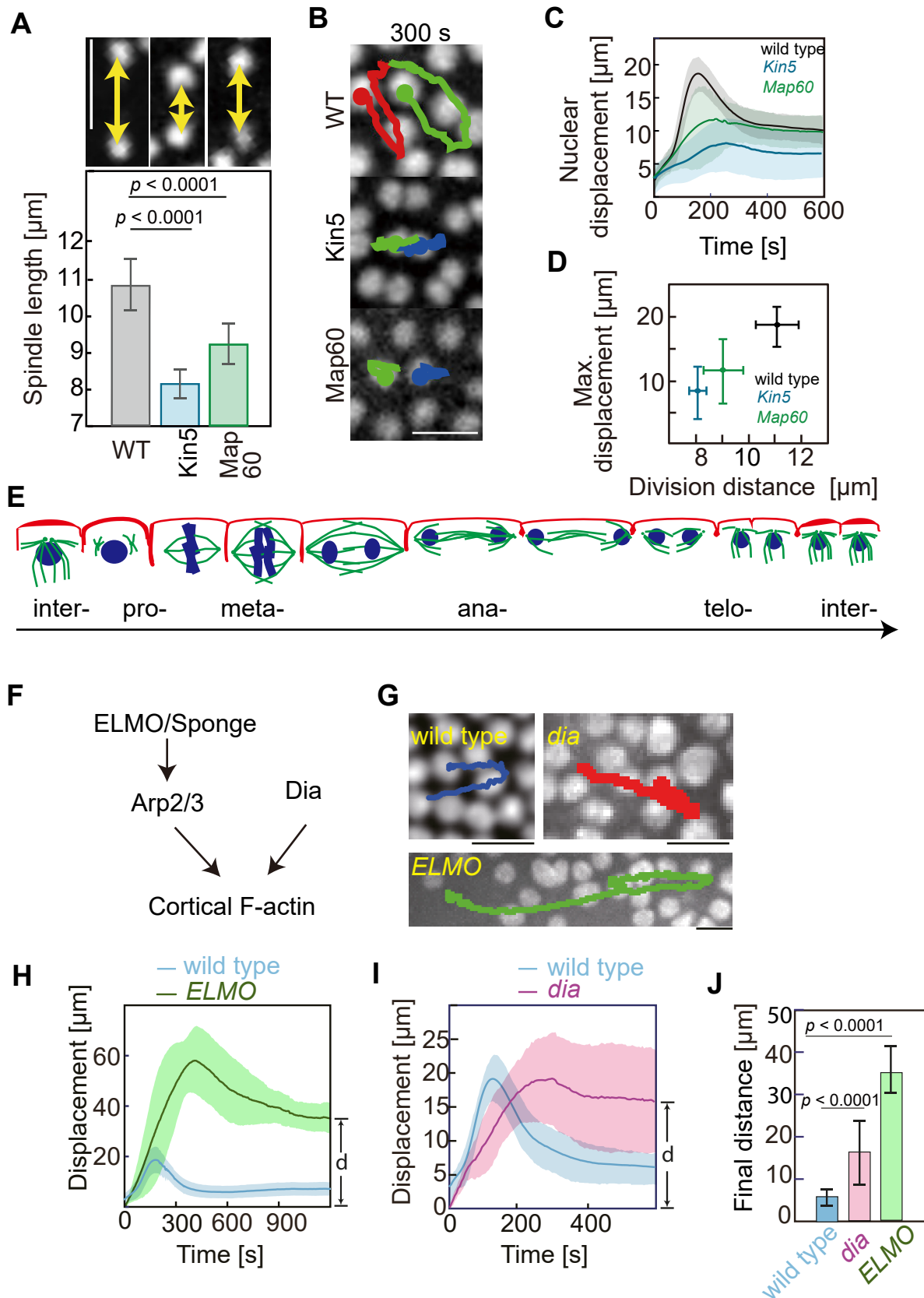


Figure 5

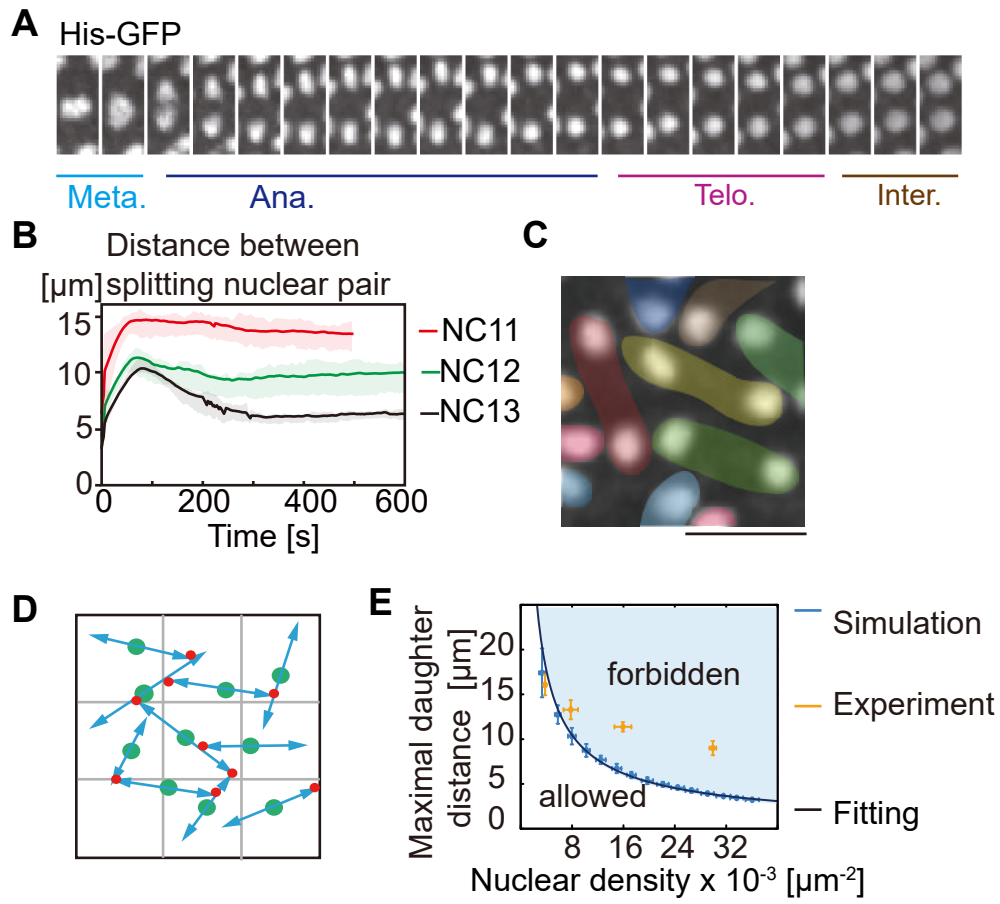


Figure S1

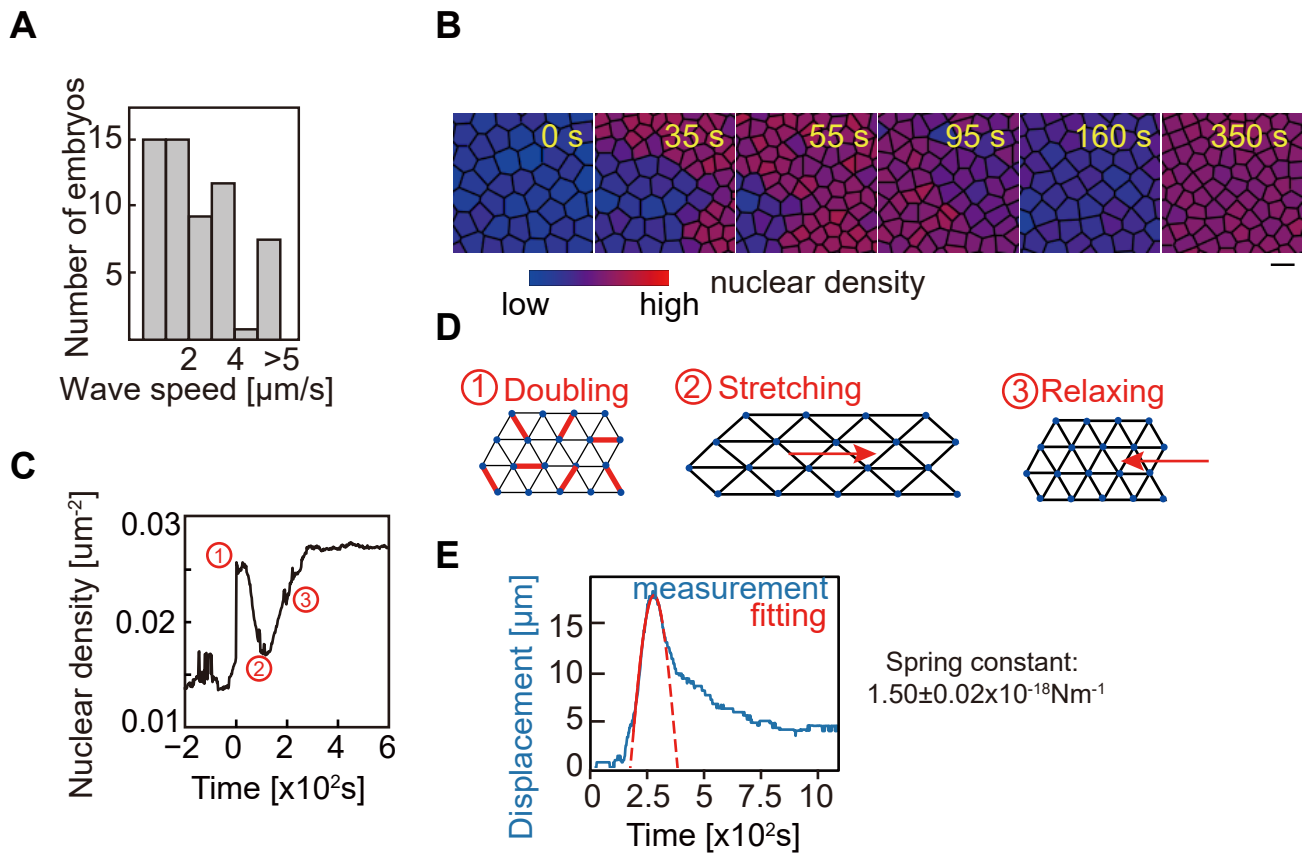


Figure S2

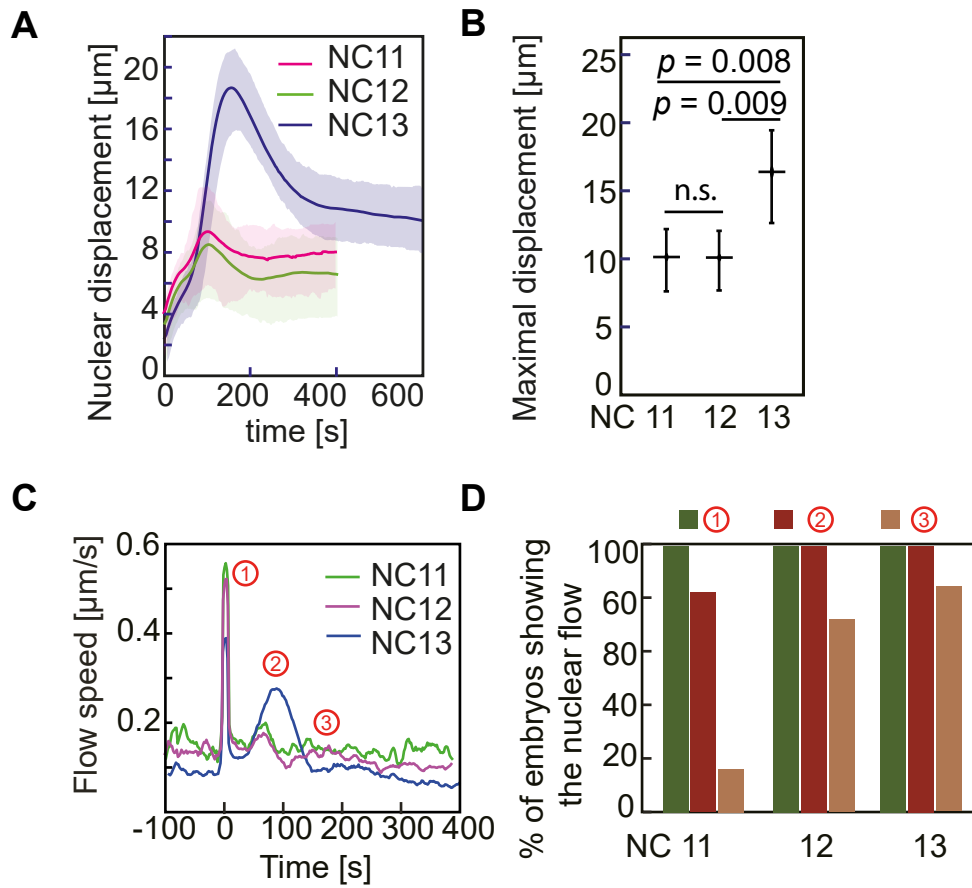


Figure S3

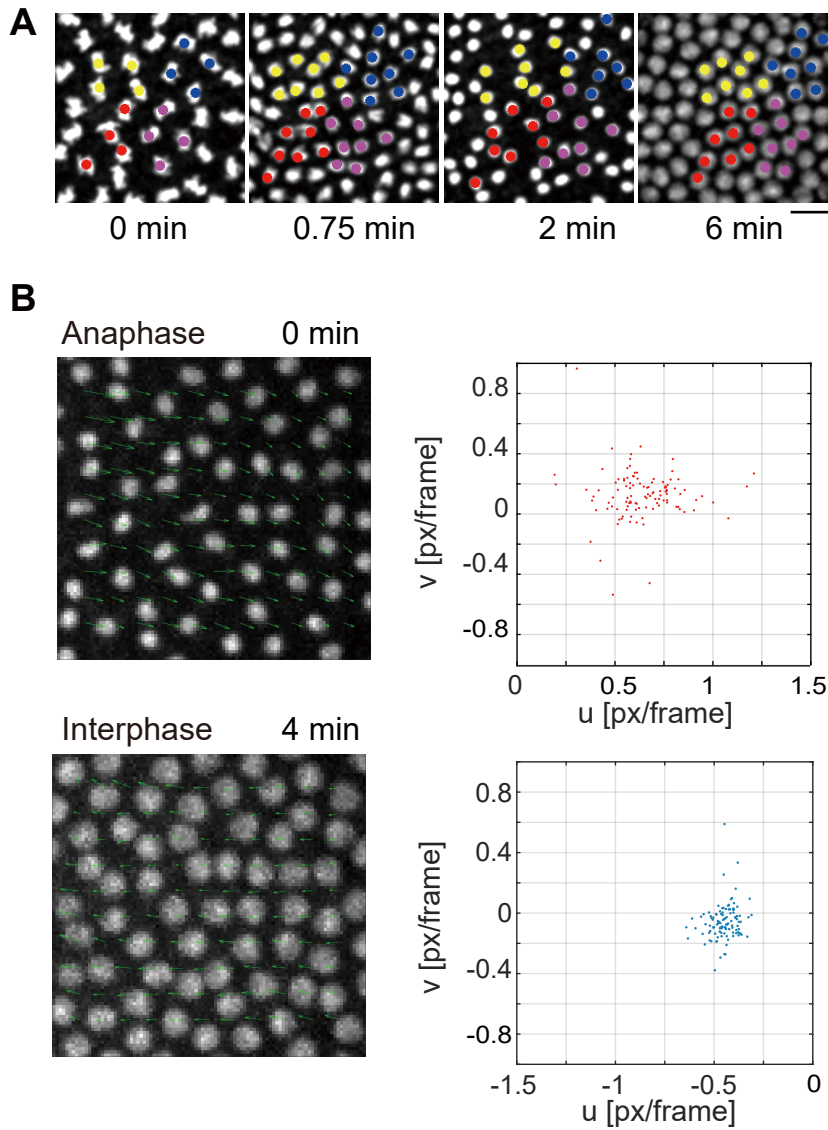


Figure S4

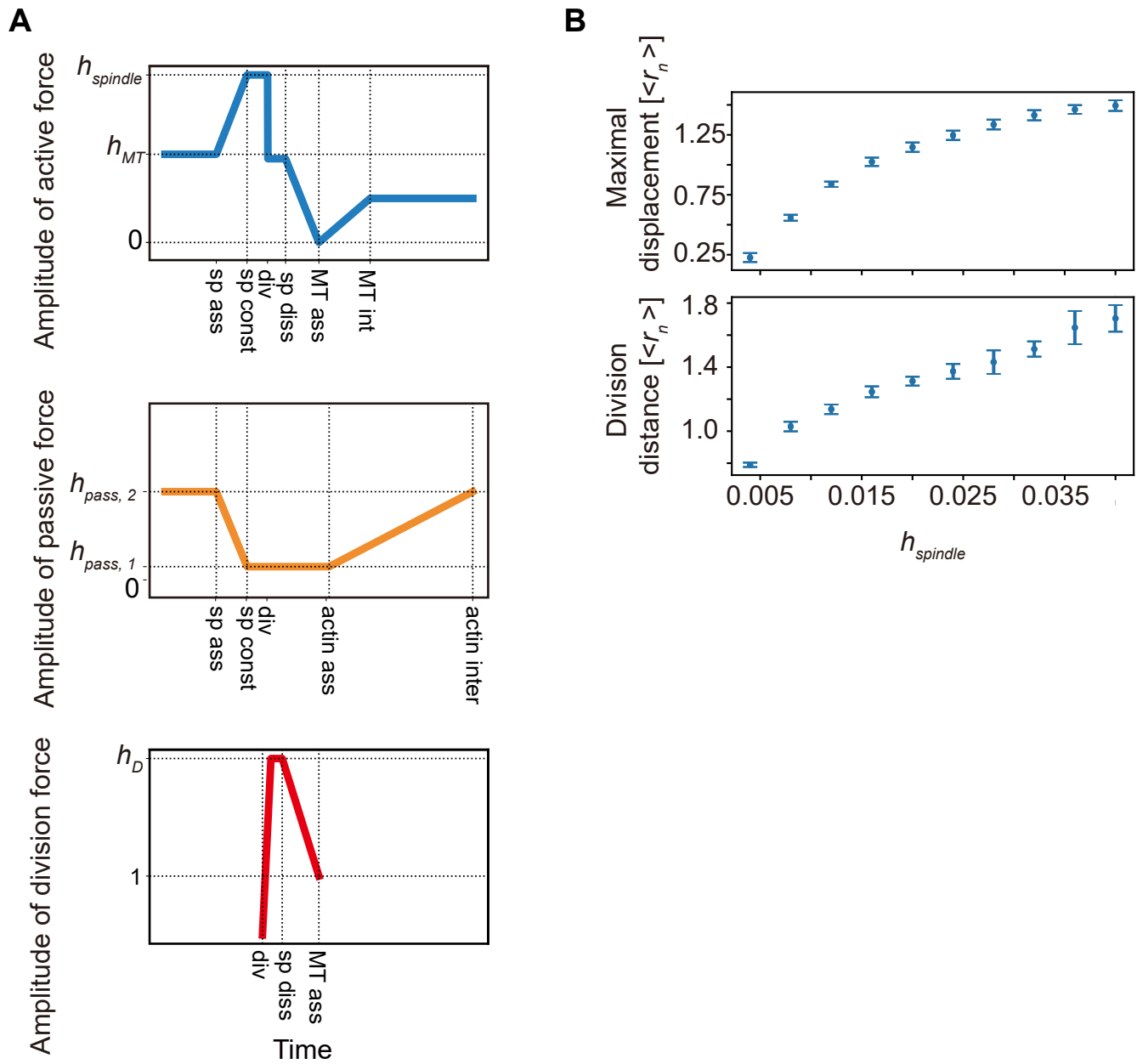


Figure S5

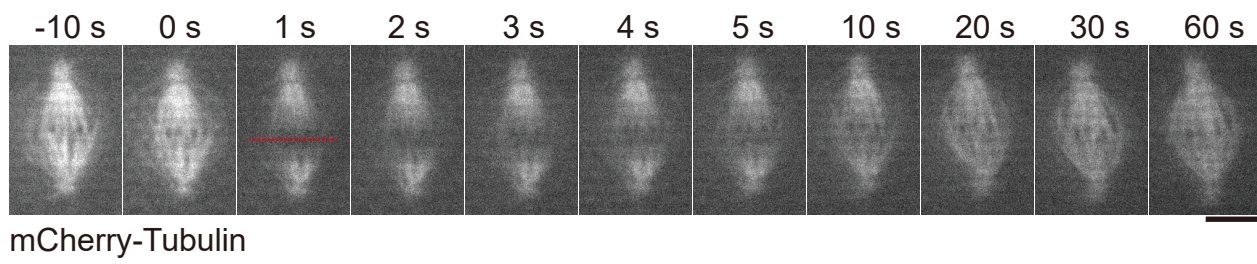


Figure S6

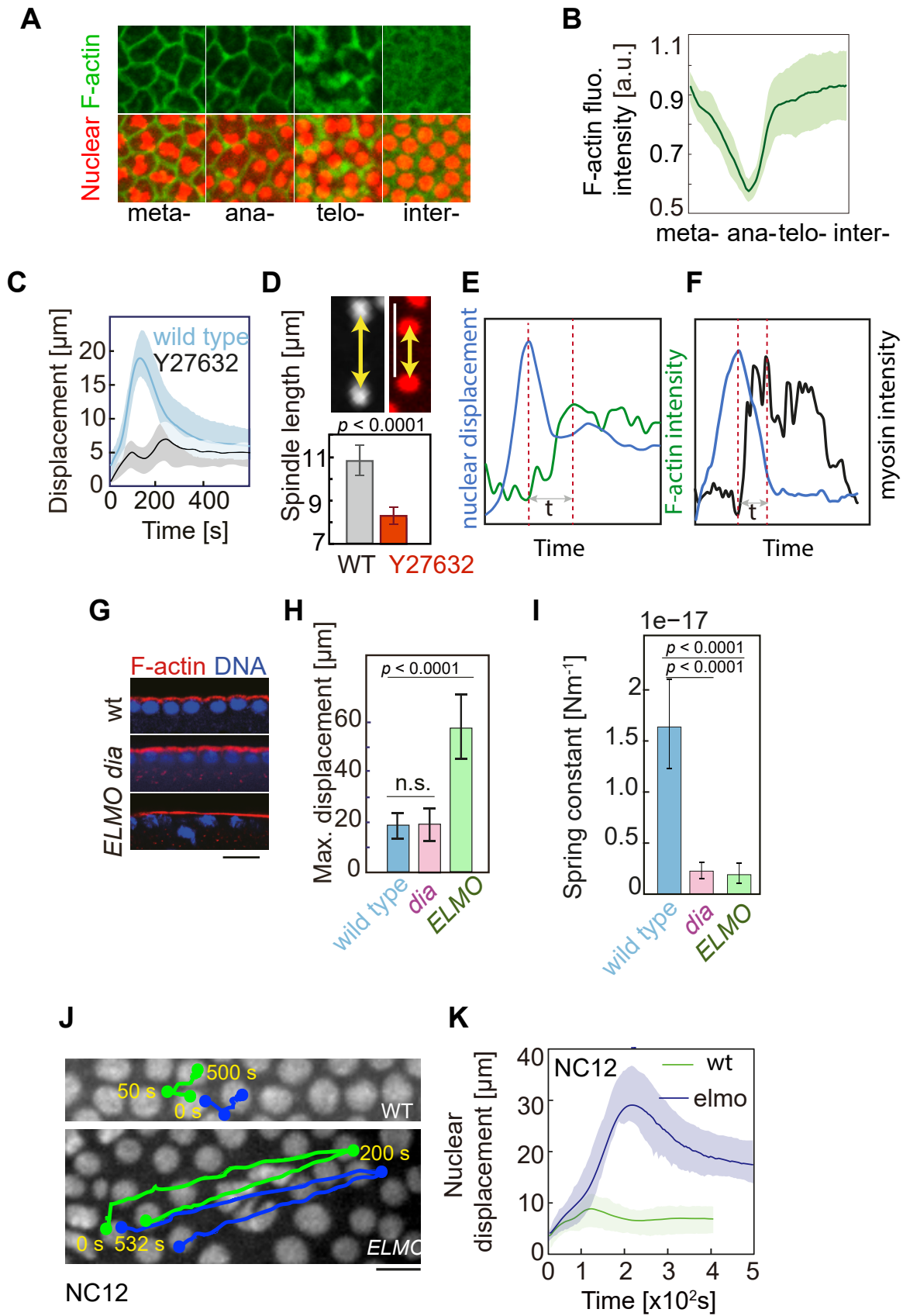


Figure S7

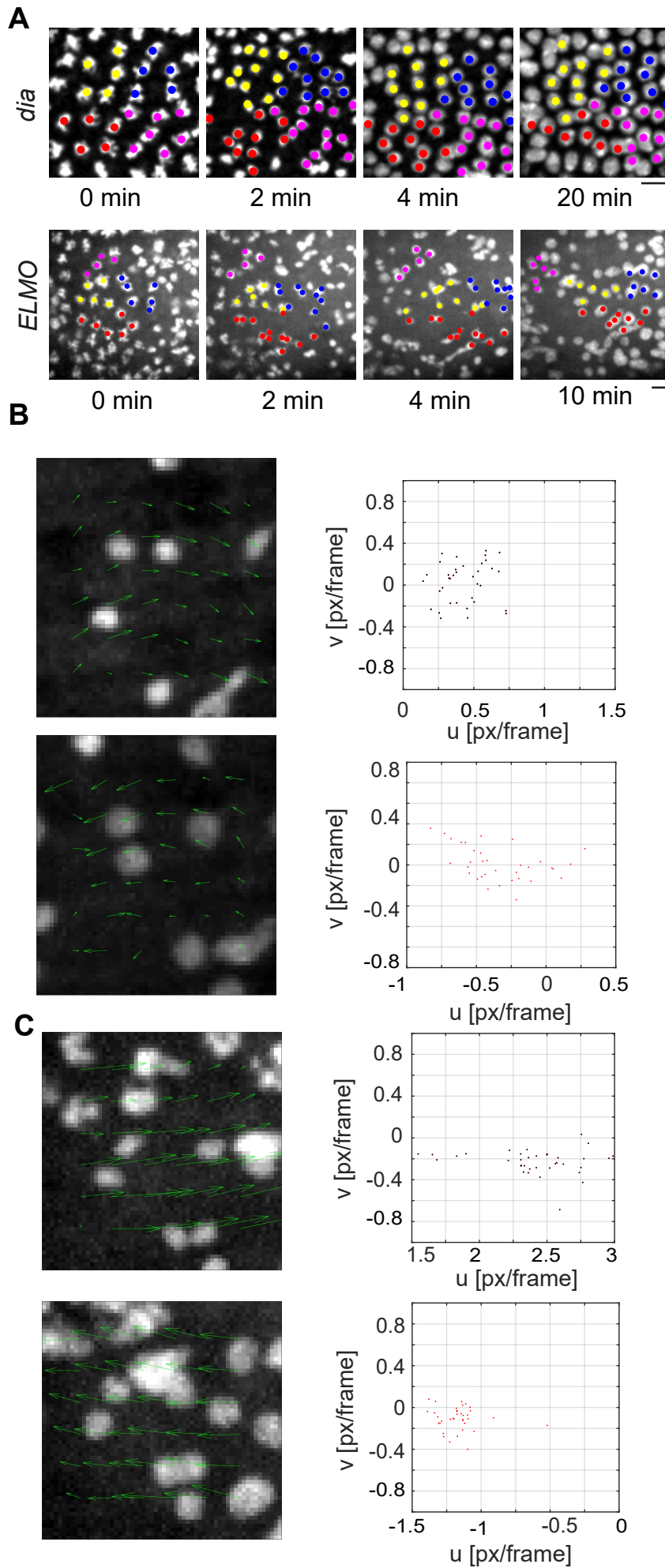


Figure S8

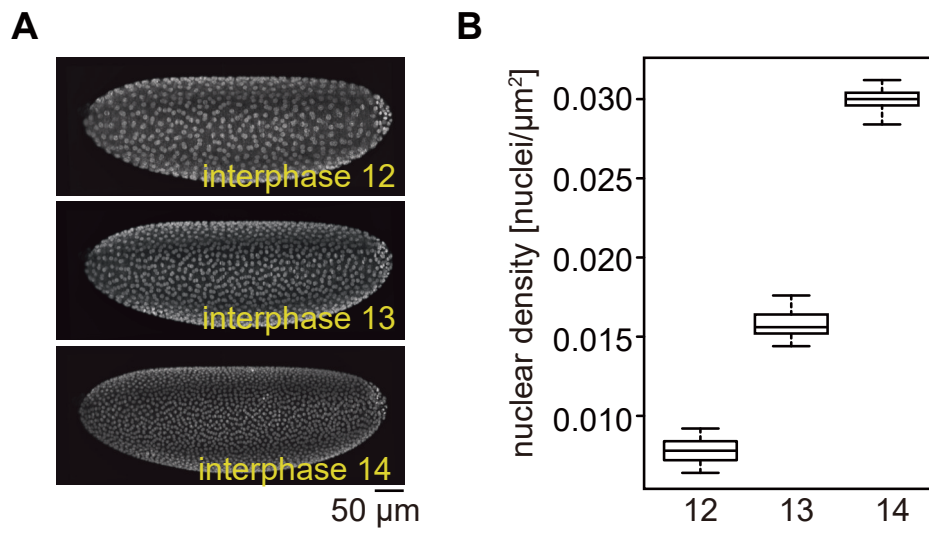


Figure S9

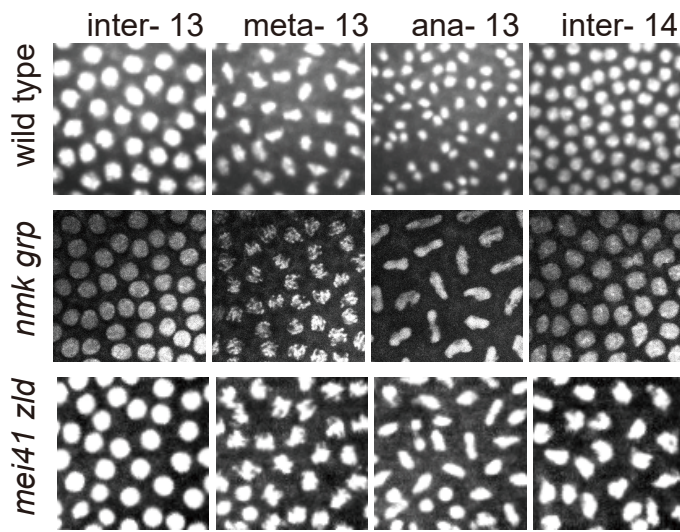


Figure S10

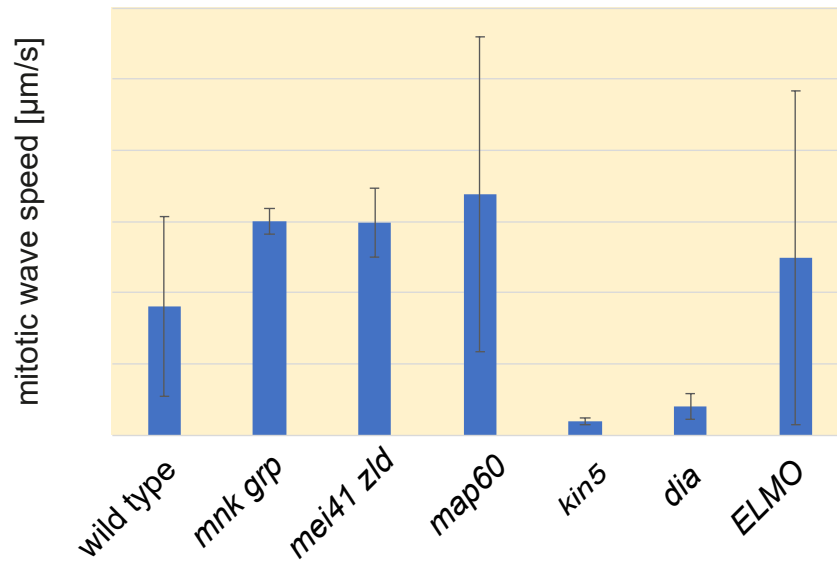


Figure S11

